



A GUIDELINE TO DERIVE OCEAN SURFACE CURRENTS FROM SPACE: AN ANALYSIS AND INTERPRETATION FRAMEWORK

Customer	ESA
Author	Consortium
Distribution	Consortium and ESA
ESA Contract Number	AO/1-7472/13/I-LG
Document Reference	TN-1
SoW Deliverable Reference	D-140
Version/Revision	2
Date of issue	29 November 2017

Issued by (NERSC)	Bertrand Chapron Ifremer Project Scientist	 King Bert
Approved by (NERSC)	Johnny A. Johannessen NERSC Project Manager	 Johnny A. Johannessen Vice Director
Approved by (ESA)	Craig Donlon ESA Technical Officer	

Revision Change log

Issue	Date	Type	Change description
0.1	3 May 2014	Initial draft	
0.2	27 May 2014	Revision	Format update
0.3	30 June 2014	Revision	Introduction update and formula numbers
0.4	10 November 2014	Revision	
0.5	10 February 2015	First version	Updated according to latest RIDS
0.6	16 December 2016	Revision	Updated according to project achievement
2	29 November 2017	Final version	Updated and Revised according to latest findings and achievements

Table of contents

1. Purpose and scope	5
1.1. Document structure.....	6
1.2. Applicable Documents.....	6
1.3. Reference documents.....	6
Publications	6
Web sites.....	8
1.4. Acronyms and abbreviations	8
2. Brief Overview	10
3. Ocean Current Terminology and Symbology	19
4. Upper Ocean Currents	23
5. Ocean Surface Current Interpretation Framework	28
6. Summary and Outlook.....	32
Annex 1: GlobCurrent Observation Framework	36
Annex A1.2: GlobCurrent data driven SST and SSH Framework.....	38
Annex A1.3: GlobCurrent Lagrangian Approach.....	41
Annex A1.4: Obuko Weiss Approach.....	44
Annex A1.5: Wave-Current Refraction.....	45
Annex A1.6: Spiraling eddies.....	46
Annex A1.7: Synergy of Mesoscale Features.....	47
Annex A1.8: Snapshot Examples from SynTool.....	48
Annex A1.9: From Symbology to Synoptic Maps.....	50

Table of figures

Figure 1: The GlobCurrent System Architecture and approach from the data and product flow, algorithm development, validation and assessment involving the broader user community to the web portal and dissemination. HRDDDS means High Resolution Dynamic Diagnostic Data Sets and extends HR-DDS to Lagrangian trajectory assessment (both in-situ and EO products derived with

time integration). HRDDDS also allows comparisons of trends (reducing impact of random errors) with respect to comparisons of snapshots.....	5
Figure 2: An initial depiction of the Gulf Stream (circulated by Benjamin Franklin, circa 1770) was constructed in part to address the question of why some ships travelling westward from England to North America made the crossing more quickly than others.....	10
Figure 3a: CNES-CLS13 mean dynamic topography: geostrophic current averaged over the years 1993 to 2012. Where altimeter observations do not provide estimates of mean geostrophic current, such as along the equator; this information is derived from buoys.	12
Figure 3b: Spiraling cyclonic eddies at scales around 10 km in the Mediterranean Sea imaged by Envisat ASAR.....	13
Figure 4: Illustration of the Lagrangian advection to dynamically interpolate large-scale tracer (ARGO surface temperature field, left) onto a high-resolution product (right). Particle trajectories computed using altimetry-derived velocities (AVISO, weekly 1/3°) with 3 hours time steps [RD-23]..	13
Figure 5: Surface roughness intense contrasts in the Mediterranean-Libyan Sea from optical sensor measurements in and around the sun glitter area, March 3 rd , 2012. Clouds are visible in the upper-right corner. The 900-nm radiance measured by the Medium Resolution Imaging Spectrometer (MERIS), on-board ENVISAT, with resolution of 250 m has been high-pass filtered at 25 km. Resulting surface contrasts evidently trace the upper ocean turbulent state.	15
Figure 6: Contemporaneous GlobCurrent geostrophic surface current velocity and Sentinel-1 SAR image on Dec 27, 2015. Rays, white trajectories, are simulating wave propagation path distorted by surface current gradient (e.g. vorticity).....	16
Figure 7: Characteristic features and processes that influence the upper ocean current. Among these are eddies, frontal boundaries, Ekman, spirals, Ekman transport, Stokes drift, turbulence, Langmuir circulation, internal waves.....	18
Figure 8: Schematic illustration of the Stokes drift and Stokes depth. The blue arrow indicates the wave propagation direction. The black arrows are instantaneous vectors marking the strength of the orbital motion of individual particles (at the surface and at different depths) induced by the propagating wave. The red loops indicate the total horizontal distance that the particles have moved over the course of 7 passing waves.....	24
Figure 9. Schematic illustration of the Langmuir circulation (first described by Langmuir, 1938). The separation scale of the convergence zones are typically 10-100 m. Courtesy Jerome Smith.....	24
Figure 10: Current profile in the upper layer induced by the Ekman spiral.....	25
Figure 11: Modification of the classical Ekman induced current spiral by Stokes drift. Circles indicate uncertainties.....	26
Figure 12: Looping trajectory of surface buoy illustrating the effect of the inertial motion following the decay of the wind forcing.....	27
Figure 13: Typical horizontal and vertical scales of key ocean surface current features related to time scales.....	28
Figure 14: Spatial and temporal scales of key upper ocean surface current features overlaid and mapped into a selection of existing and future approved and planned satellite duty cycles and sampling coverage typical representative for mid-latitudes.....	33
Figure A1.1: Illustration of Sentinel-1, -2 and -3 provision of data and information products in support to the global, regional and local surface current estimations. Additional provision of complementary data and information from supporting missions (e.g. SMOS and GOCE) and in-situ data further demonstrates the importance and strength of the systematic use of sensor synergy.	36
Figure A1.2: Mean SSH gradients (upper) and SST gradients (lower) for February 2008.	39
Figure A1.3: Surface currents derived from altimeter SSHs and (a) microwave SSTs and (b) the associated temperature gradient norms within the Agulhas return current on January 1, 2004.	40
Figure A1.4: Synoptic snapshot of the so-called “dog head” feature showing the combined 2-D SST map (colour), surface geostrophic current (stippled streamlines), and surface roughness from the Sentinel-1 SAR image obtained on 23 March 2015. The sea surface height track data from radar altimetry are also overlaid. The color bar gives the SST in degree Celsius.....	41
Figure A1.5: Illustration of Lagrangian advection in the Gulf Stream region to dynamically interpolate medium-scale surface temperature (passive microwave AMSR-E surface temperature field, bottom left) onto a high-resolution product (bottom right). Backward particle trajectories computed	

using altimetry-derived velocities (AVISO, weekly 1/3°) with 3 hours time steps to compare with previous observations (12 days backward), i.e. high-resolution MODIS sea surface temperature (top, left) and medium-resolution AMSR-E sea surface temperature (top, right)	42
Figure A1.6: Contemporaneous sea surface temperature fields from MODIS (upper left) at 2 km resolution, and AMSR-E (upper right) at 25 km sampling resolution. Spectral analysis (lower) illustrates the impact of instrumental smoothing effect on AMSR-E (passive microwave) observations to strongly increase the spectral roll-off, starting at 100 km scale. Comparisons are given with filtered and non-filtered MODIS observations.	43
Figure A1.7: Contemporaneous GlobCurrent geostrophic surface current velocity and Sentinel-1 SAR image on Dec 27, 2015. White trajectories are simulated wave propagation path distorted by surface current vorticity. Red rectangle highlights the area of resulting crossing swell detailed on Figure A1.8.	45
Figure A1.8: Swell propagation path simulated using GlobCurrent geostrophic current (left) and observed on Sentinel-1 SAR (right) overlaid on Sentinel-1 sea surface roughness map acquired on Dec. 27, 2015.	46
Figure A1.9: Train of spiraling cyclonic eddies in the Agulhas Return Current imaged by Sentinel-1 SAR on 21 November 2016. Note also the bright ship with the discontinuous ship track passing through the center of one of the spirals. Spiral sizes are 15-25 km.	46
Figure A1.10: Multi-sensor expressions of a mushroom like eddy pair with a diameter of 120 km. MODIS SST map (a) and surface current divergence field derived from the SST field (b). The MSS contrasts derived from the MODIS (c) and the ASAR NRCS contrast (d). The NRCS contrasts are in linear units. Bright areas in the upper-right plot correspond to the current convergence, and dark – to	
Figure A1.11a: Collocated Chl-A concentration and SST field from VIIRS radiometer showing negative correlation in the Benguela coastal upwelling region.	48
Figure A1.11b: Collocated Chl-A concentration and SST field from MODIS radiometer showing positive correlation in the eddies shed from the Agulhas Return Current into the Antarctic Circumpolar Current.	49
Figure A1.12: The western Mediterranean Sea has a variety of features that can be used to optimize ship routing. Part of the challenge is to extract high-level features of interest such as water-type boundary fronts and significant currents of interest for a particular ship voyage. This image shows sea-surface temperature overlaid with GlobCurrent streamlines. The white broken line shows the planned passage of a ship that takes advantage of ocean-surface currents	50.

List of tables

Table 1: Surface current types observed in the near surface layer and their corresponding measured quantities, sampling requirement and requirement for auxiliary information	19
Table 2: Ocean current classification	21
Table 3: Ocean current symbology	22
Table A1.1: Observational platforms and the corresponding ocean surface current component information that can be observed	38

1. Purpose and scope

The purpose of this Technical Note (TN) is to outline an analysis and interpretation framework for Ocean Surface Current (OSC) estimates primarily using different satellite observations complemented, when possible, with *in situ* measurements. In so doing it moreover provides a comprehensive specification of nomenclature and symbology along with methods that can be used to produce the best possible gridded products to meet various user needs. It was anticipated that the TN would evolve during the course of the GlobCurrent project in consultation with the user community and expert users, and with the intention of remaining consistent with GlobCurrent product improvements (both in substance and form), including metadata (at both discovery/collection and file granularity level), uncertainty estimates, auxiliary data, and flags. Accordingly, this updated document follows the user consultation meetings in the last quarters of 2015 and 2017 as well as the most recent GlobCurrent project achievements and findings.

The document is consistent with the project architecture shown in Figure 1, which includes: (in blue) data ingestion, formatting, quality control, and processing to L2 and L4 products and connected with a Web portal; (in brown) a data management system for all data within the project (i.e. the input EO and *in situ* data, products, validation reports, etc); (in purple) validation that are strongly coupled to (in dark green) user-led case studies; and finally (in light green) a data delivery communication and system interfaced to users.

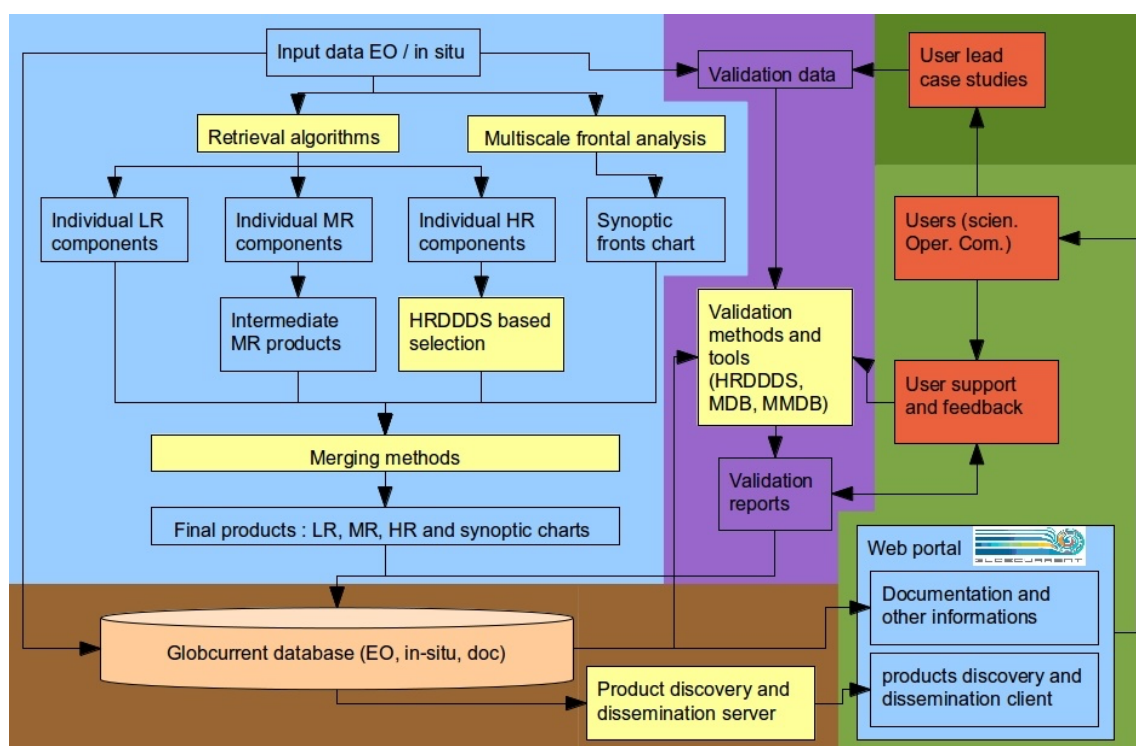


Figure 1: The GlobCurrent System Architecture and approach from the data and product flow, algorithm development, validation and assessment involving the broader user community to the web portal and dissemination. HRDDDS means High Resolution Dynamic Diagnostic Data Sets and extends HR-DDS to Lagrangian trajectory assessment (both *in-situ* and EO products derived with time integration). HRDDDS also allows comparisons of trends (reducing impact of random errors) with respect to comparisons of snapshots.

An important objective of this project, as given by its users, is validation and estimation of data quality (e.g., errors and flags; Fig. 1 purple), given observations that are independent of the analyses. Assessment of a GlobCurrent surface current (component and or combined) can

also be performed in part using assimilation systems (e.g., MyOcean) as a reference. However, because assimilation systems also depend on ocean models [RD-3; RD-4] that have limited vertical resolution near the surface, they are not expected to be a reference for all the fast current variations that GlobCurrent aims to resolve. A complementary assessment of current including fast variations is also possible using independent in situ observations (e.g., Argo and surface drifters), and high-resolution remote sensing (e.g., satellite optical glitter and land-based high frequency radar) as shown by [RD-1; RD-2]. User led case studies (Fig.1 dark green) provide opportunities to pursue this objective at the GlobCurrent supersites (e.g., over the Agulhas Current regions).

Further details on architecture are provided in the latest versions of the GlobCurrent project's Requirements Baseline (RB) and Technical Specification (TS) documents. Here, we provide the scientific basis for these documents and a motivation for our choice of upstream input data, processing chains and retrieval algorithms, and derived products at scales from global (low resolution) to local (high resolution).

1.1. Document structure

This document is organized into the following sections:

- Section 1 (this section) outlines the scope and structure of the document
- Section 2 provides a brief introduction
- Section 3 provides a an introduction to ocean current terminology
- Section 4 addresses the upper ocean surface current components
- Section 5 identifies the reference depths and definitions
- Section 6 is a summary
- Annex 1 provides the nomenclature and observational and analysis framework for all products

1.2. Applicable Documents

1.3. Reference documents

The following are the publications and web sites relevant to this document.

Publications

- [RD-1] Bonjean F. and G.S.E. Lagerloef, 2002, Diagnostic Model and Analysis of the Surface Currents in the Tropical Pacific Ocean, *J. Phys. Ocean.*, 32, 2938-2954.
- [RD-2] Rio, M.-H., S. Mulet, and N. Picot, 2014, Beyond GOCE for the ocean circulation estimate: Synergetic use of altimetry, gravimetry, and in situ data provides new insight into geostrophic and Ekman currents, *Geophys. Res. Lett.*, 41, 8918–8925
- [RD-3] Larnicol, G., Guinehut, S., Rio, M.-H., Drevillon, M., Faugere, Y., and Nicolas, G. 2006, The global observed ocean products of the French Mercator project, in: Proceedings of the “15 years of progress in radar altimetry” ESA Symposium, ESA, Venice, 2006.
- [RD-4] Madec G. 2008: "NEMO ocean engine". Note du Pole de modélisation, Institut Pierre-Simon Laplace (IPSL), France, No 27 ISSN No 1288-1619
- [RD-5] Fu, L.-L., D.B. Chelton, P.-Y. Le Traon, and R. Morrow. 2010. Eddy dynamics from satellite altimetry. *Oceanography*, Vol. 23, pp. 14–25, doi:10.5670/oceanog.2010.02.

- [RD-6] Breivik, Ø. and A. A. Allen, 2008, An operational search and rescue model for the Norwegian Sea and the North Sea, *J. Mar. Systems*, Vol. 69, pp. 99-113, ISSN 0924-7963
- [RD-7] Breivik, Ø., A. A. Allen, C. Maisondieu, and J. C. Roth, 2011, Wind-induced drift of objects at sea: The leeway field method, *Appl. Ocean Res.*, Volume 33, pp. 100-109, ISSN 0141-1187.
- [RD-8] Kudryavtsev, V. N. A. Myasoedov, B. Chapron, J. A. Johannessen, F. Collard, (2012), Imaging mesoscale upper ocean dynamics using SAR and optical data, *Journal of Geophysical Research*, Vol. 117, C04029, 2012.
- [RD-9] A.R. Robinson, (1983) Eddies in Marine Science, *Springer-Verlag*, Beling Heidelberg.
- [RD-10] Kamenkovich V. M., M. N. Koshlyakov, and A.S. Monin, (1986) Synoptic Eddies in the Ocean, *Kluwer Academic publishers*.
- [RD-11] D. B. Chelton (2001), Report of the high-resolution ocean topography science working group meeting.
- [RD-12] Arduin F., L. Marié, N. Rascle, P. Forget, and A. Roland, 2009: Observation and Estimation of Lagrangian, Stokes, and Eulerian Currents Induced by Wind and Waves at the Sea Surface. *J. Phys. Oceanogr.*, **39**, 2820–2838.
- [RD-13] McWilliams J. C., E. Huckle, and A. F. Shchepetkin, 2009: Buoyancy Effects in a Stratified Ekman Layer. *J. Phys. Oceanogr.*, **39**, 2581–2599.
- [RD-14] Kudryavtsev V. N. and A. V. Soloviev, 1990: Slippery Near-Surface Layer of the Ocean Arising Due to Daytime Solar Heating. *J. Phys. Oceanogr.*, **20**, 617–628.
- [RD-15] Pedlosky J., 2008: On the Weakly Nonlinear Ekman Layer: Thickness and Flux. *J. Phys. Oceanogr.*, **38**, 1334–1339.
- [RD-16] Klein P. and B.-L. Hua, 1988, Mesoscale heterogeneity of the wind-driven mixed layer: Influence of a quasigeostrophic flow. *Journal Of Marine Research*, 46(3), 495-525
- [RD-17] Garrett, C. J. R., and J. W. Loder (1981), Dynamical aspects of shallow sea fronts, *Philos. Trans. R. Soc. London, Ser. A*, 1981, 563–581.
- [RD-18] Lapeyre G. and P. Klein, 2006: Dynamics of the Upper Oceanic Layers in Terms of Surface Quasigeostrophy Theory. *J. Phys. Oceanogr.*, **36**, 165–176.
- [RD-19] Isern-Fontanet, J., B. Chapron, G. Lapeyre, and P. Klein, 2006, Potential use of microwave sea surface temperatures for the estimation of ocean currents, *Geophys. Res. Lett.*, 33, L24608.
- [RD-20] Dohan, K., and N. Maximenko. 2010. Monitoring ocean currents with satellite sensors. *Oceanography*, 23(4):94–103, doi:10.5670/oceanog.2010.08.
- [RD-21] Reul, N., B. Chapron, T. Lee, C. Donlon, J. Boutin, and G. Alory, 2014, Sea surface salinity structure of the meandering Gulf Stream revealed by SMOS sensor, *Geophys. Res. Lett.*, 41, 3141–3148.
- [RD-22] Ponte A. L., P. Klein, X. Capet, P.-Y. Le Traon, B. Chapron, and P. Lherminier, 2013: Diagnosing Surface Mixed Layer Dynamics from High-Resolution Satellite Observations: Numerical Insights. *J. Phys. Oceanogr.*, **43**, 1345–1355.
- [RD-23] Lumpkin, R., and G. C. Johnson, 2013, Global ocean surface velocities from drifters: Mean, variance, El Nino–Southern Oscillation response, and seasonal cycle, *J. Geophys. Res. Oceans*, 118, 2992–3006
- [RD-24] Dencausse G., R. Morrow, M. Rogé, S. Fleury, 2014, Lateral stirring of large-scale tracer field by altimetry, *Ocean Dynamics*, 61, 1, 61-78.

- [RD-25] Tandéo P., B. Chapron, S. Ba, E. Autret, R. Fablet, 2014, Segmentation of Mesoscale Ocean Surface Dynamics Using Satellite SST and SSH Observations. *IEEE TGRS*, 52(7), 4227-4235.
- [RD-26] Lesieur M. and R. Sadourny, 1981, Satellite-sensed turbulence ocean structure, *Nature*, 294, 673. Chae D., P. Constantin, J. Wu, 2012, Deformation and symmetry of the inviscid SQG and the 3D Euler equations, *J. Nonlin. Scien.*, 22, 665-688.
- [RD-27] Munk, W., L. Armi, K. Fischer and F. Zachariasen (2000), *Proc. R. Soc. Lond. A* 456, 1217-1280
- [RD-28] Johannessen, J. A., B. Chapron, F. Collard, B. Backeberg, 2014, Use of SAR data to monitor the Greater Agulhas Current, *In Remote Sensing of the African Seas*, edited by V. Barale and M. Gade, ISBN 978-94-017-8007-0, Springer.
- [RD-29] Raj, R.P., J. A. Johannessen, T. Eldevik, J. E. Ø. Nilsen, I. Halo, (2016) Quantifying mesoscale eddies in the Lofoten Basin, *Journal of Geophys. Res.*
- [RD-30] Arduin, Fabrice, Sarah T. Gille, Dimitris Menemenlis, Cesar B. Rocha, Nicolas Rasle, Bertrand Chapron, Jonathan Gula, Jeroen Molemaker (2016), Small-scale open-ocean currents have large effects on ocean wave heights, *Journal of Geophys. Res.-Oceans*, 2017.
- [RD-31] Bentamy, A. J. F. Piollé, A. Grouazel, R. Danielson, S. Gulev, F. Paul, H. Azelmat, P.P. Mathieu, K. Von Schuckmann, S. Sathyendranah, H. E. King, I. Esau, J. A. Johannessen, C. A. Clayson, R. T. Pinker8, S. Grodsky, M. Bourassa, S. R. Smith, K. Haines, M. Valdivieso, C. J. Merchant, B. Chapron, A. Anderson, R. Hollmann, and S. A. Josey (2017), Towards Improved Estimation of Turbulent Heat Flux over the Global Oceans, *Remote Sensing of Environment*, 2017.
- [RD-32] Isern-Fontanet, J., E. Olmedo, A. Turiel, J. Ballabrera-Poy, and E. García-Ladona (2016), Retrieval of eddy dynamics from SMOS sea surface salinity measurements in the Algerian Basin (Mediterranean Sea), *Geophys. Res. Lett.*, 43, doi:10.1002/2016GL069595.
- [RD-33] Rasle Nicolas, Molemaker Jeroen, Marie Louis, Nouguier Frederic, Chapron Bertrand, Lund Bjorn, Mouche Alexis (2017). Intense deformation field at oceanic front inferred from directional sea surface roughness observations. *Geophysical Research Letters*, <http://doi.org/10.1002/2017GL073473>

Web sites

- [WEB-1] GlobCurrent external web site <http://www.globcurrent.org>
- [WEB-2] GlobCurrent internal web site <http://globcurrent.nersc.no>
- [WEB-3] [ODL web site](http://odl.oceandatalab.com) <http://odl.oceandatalab.com>
- [WEB-4] DUE web site <http://due.esrin.esa.int>

1.4. Acronyms and abbreviations

AATSR	Advanced Along Track Scanning Radiometer (of ENVISAT)
ADB	Actions Data Base
AMSRE	Advanced Microwave Scanning Radiometer – E (of EoS Aqua)
AQUARIUS	Salinity mission (of NASA/CONAE)
ASAR	Advanced Synthetic Aperture Radar (of ENVISAT)
ASCAT	Advanced SCATterometer (of MetOp)
ATBD	Algorithm Theoretical Basis Document
AVHRR	Advanced Very High Resolution Radiometer
CDR	Critical Design Review
DIR	Directory (of project participants)

DMSP	Defense Meteorological Satellite Program (of the USA)
ENVISAT	Environnent Satellite (http://envisat.esa.int)
ESA	European Space Agency
EO	Earth Observation
EU	European Union
FR	Final Report
Hs	Significant Wave Height (also SWH)
ITT	Invitation To Tender
KO	Kick-Off
MR	Monthly Report
MTR	Mid-Term Review
NOP	Numerical Ocean Prediction
NWP	Numerical Weather Prediction
OSC	Ocean surface current
PAR	Preliminary analysis report
PM	Progress meeting
PMP	Project Management Plan
PMR	Passive Microwave Radiometry
RA-2	Radar Altimeter 2 (of ENVISAT)
RB	Reference Baseline
RD	Reference Document
SAR	Synthetic Aperture RADAR
SAR	Scientific Assessment Report (of SOS)
SAP	Scientific Analysis Plan
SIAR	Scientific and Impact Assessment Report
SMOS	Soil Moisture and Ocean Salinity (mission)
SOS	Surface Ocean Salinity and Synergy (project)
SoW	Statement of Work
SRR	System Requirements Review
SSH	Sea Surface Height
SSM/I	Special Sensor Microwave Imager (of DMSP)
SST	Sea Surface Temperature
SR	Scientific Roadmap
STSE	Support to Science Element
TBC	To Be Confirmed
TBD	To Be Determined
TDP	Technical Data Package
TDS	Test Data Set
TN	Technical Note
TOA	Top of Atmosphere
TR	Technical Report
UCM	User Consultation Meeting
UM	User Manual
URD	User Requirements Document
URL	Universal Resource Locator
WP	Work Package

2. Brief Overview

Our ability to monitor ocean currents and to understand the fundamental processes that shape them is evolving. It is not surprising, therefore, that the contemporary definition of a current has evolved as well. From a purely physical point of view, an ocean surface current can be characterized as *a coherent horizontal and vertical movement of water – in contact with the surface and over a specific depth regime – with a given velocity that persists over a region and time period*. Although the motivation for understanding great ocean currents has its source in traditional maritime activities like transportation and shipping (Fig. 2), societal interests have continued to broaden. For example, we now regularly perform search and rescue operations, monitor sediment transport and pollution dispersal, and predict fish egg and larvae drift, or the global distribution and transport of marine plastics. In turn, the modern definition of an ocean current now encompasses smaller scales and their associated three-dimensional flows, with manifestations at the surface that are just beginning to be resolved and interpreted.

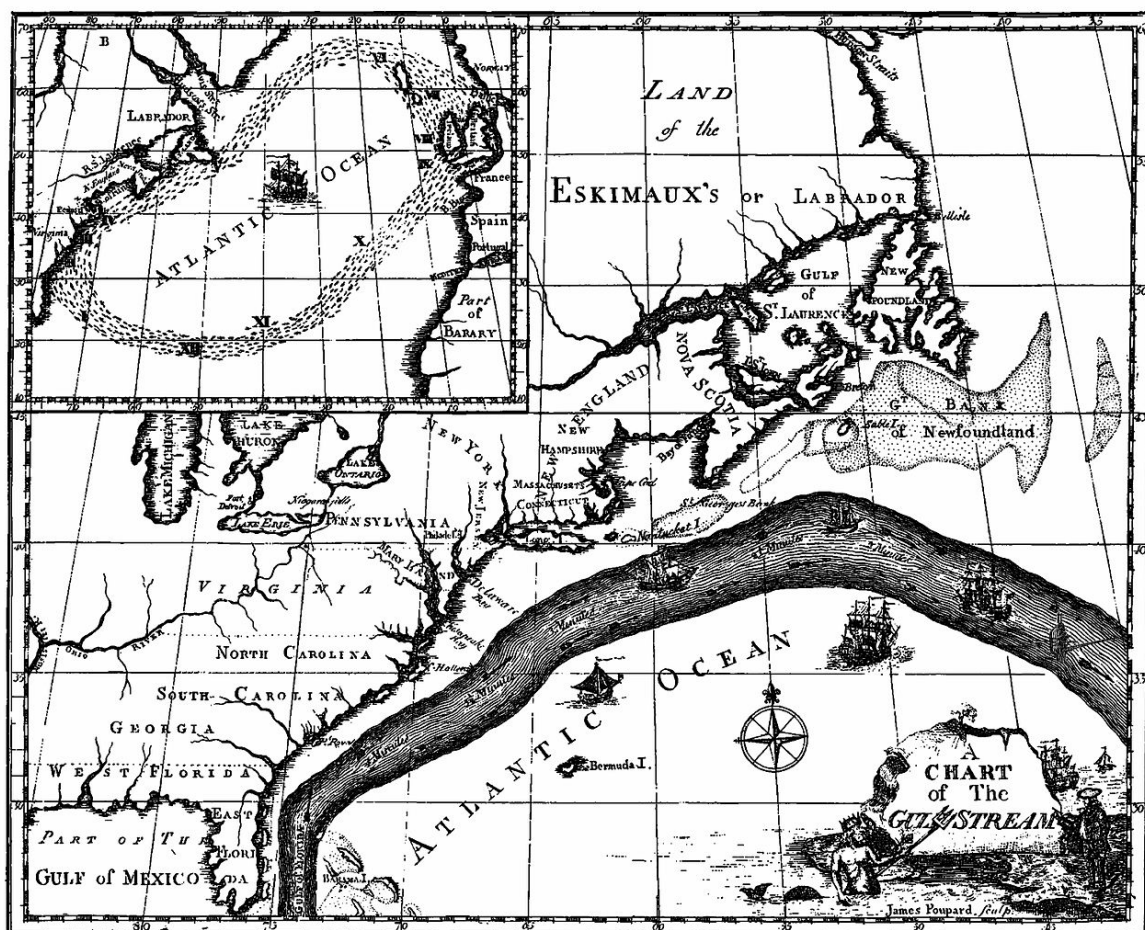


Figure 2: An initial depiction of the Gulf Stream (circulated by Benjamin Franklin, circa 1770) was constructed in part to address the question of why some ships travelling westward from England to North America made the crossing more quickly than others.

Mariners initially had to rely on their own observations to map what is now called a mean surface current (Fig. 2). More recent decades have witnessed the deployment of an increasingly diverse set of satellite and buoy platforms, along with two significant advances: a synergetic use of these observations and the discovery of ocean eddies. The 1960's marked

some of the first coordinated *in situ* measurement campaigns that began to resolve individual mesoscale eddies and an eddy impact on the total flow was first confirmed [RD-9; RD-10]. In equilibrium, the pressure gradients that cause the ocean's circulation are balanced with the forces of gravity and the Coriolis force due to Earth's rotation. Subsequent studies, based on multiple altimeters that provided decades of truly synoptic sea level observations, concluded that most of the kinetic energy of the ocean is indeed defined by its eddy currents (cf. [RD-5]). Coherent eddy structures (> 100-200 km) with lifetimes from weeks to years (Chelton et al., 2011), the building blocks of the Ocean Weather, are thus now known to contain almost 90% of the total kinetic energy (KE) of the flow, described with a quasi-universal empirical wavenumber-frequency spectrum model (Wortham and Wunsch, 2014). Yet, a full knowledge of the ocean dynamics remains fundamentally incomplete, and the associated practical problem to understand and predict lateral eddy fluxes of heat, salt and material properties remains largely unsolved. At shorter horizontal scales (< 50 km), nonlinearity comes into play, bringing more complex dynamics. A wider range of scales must thus be resolved in order to answer practical questions, such as what determines the drift of a buoyant object at sea (e.g. [RD-6; RD-7]). The growth of observational diversity over the years also implies that the synergetic use of surface current information is an important challenge for the GlobCurrent project and beyond.

Because of this multitude of types of coherent structures and its great hierarchy in space and time scales (in size and period), the circulation dynamics of the ocean can be said to be "multi-scale" in space and time. It is thus essential to complement satellite altimetry, and the last decade or two of EO has seen efforts to help retrieve ocean surface current information from different measurements and advanced interpretation strategies. The arrival of the Sentinel era finds some techniques that are mature (e.g. altimetry, ocean surface temperature fronts, optical feature tracking), while new satellites (e.g. GOCE, Cryosat, SMOS) and techniques have emerged (e.g. SAR radial velocities, swell ray tracing, mean square slope from glitter patterns, improved geoid models) that promise additional capabilities to resolve small scale ocean surface currents. This combination of established and newer techniques represents a rich infrastructure for building the ocean services of the future. Among numerous operational analyses and historical reanalyses of the ocean surface current (both global and local), GlobCurrent is also seeking to lead the exploitation of instantaneous, e.g. snapshot, EO information.

To recall, since the first images from space, the attention of both theoreticians and remote sensing scientists has strongly been triggered by the abundance of various ocean tracer patterns and signatures in the mesoscale and sub-mesoscale (1-50 km) ranges. In particular, intriguing small cyclonic spiral eddies (see Figure 3b), with scales 5-10 km, are not rare events, with "almost ubiquitous occurrence ... whenever submesoscale dynamics was revealed in the sun glitter" (from Scully-Power, 1986, page 62 Navy Oceanographer shuttle observations). As often detected, filamentary and spiral structures are 2D surface expressions of upper ocean 3D tracer anomalies with varying depths and tilts. Needless to say, the use of tracer information to estimate surface displacements has certainly a long history in physical oceanography. Sequences of high-resolution IR images have, for instance, been successfully used (e.g. Bowen et al., 2002, Matthews and Emery, 2009). Among different techniques, the Maximum Cross Correlation (MCC) method to identify pattern displacements is by far the most widely used. Other methods can be invoked, such as constrained optical flow methods to solve the heat equation (e.g. Kelly, 1989; Vigan et al., 2000), possibly combined with a priori background information (e.g. Mercantini et al., 2010, Piterbarg and Ivanov, 2013, Rio et al., 2016)). To gain resolution, these techniques generally rely on the availability of cloud-

free images with short-time intervals between acquisitions, and favours sampling from geostationary rather than polar-orbiting satellites (Warren et al., 2016).

To date, the cloud-free constraint precludes global systematic and direct quantification of horizontal transport and dispersion, and mixing at small scales (< 50 km) is still beyond reach. Yet, as mentioned above, from precise measurements of the ocean topography and its related dynamics, significant progresses have been made.

Indeed, satellite altimetry is arguably the most mature technique for mapping balanced motions and has led to breakthroughs in our understanding of the dynamics of large-scale (roughly $>100 - 200$ km) oceanic circulation with unequalled views of eddy kinetic energy on a global scale as shown in Figure 3a. Because of the narrow illuminated swath of present instrument, regardless of the orbital configuration, conventional ground track spacing of an individual altimeter is coarse and known to limit cross-track resolution. The ocean's mesoscale (30-100 km) and submesoscale ($< 10-30$ km) variability and energy are thus almost impossible to map with conventional radar altimeters (see Figure 3b). Even combined, multiple altimeter measurements yield gridded maps of sea surface height (SSH) limited to a resolution of about 100 km and 10 days.

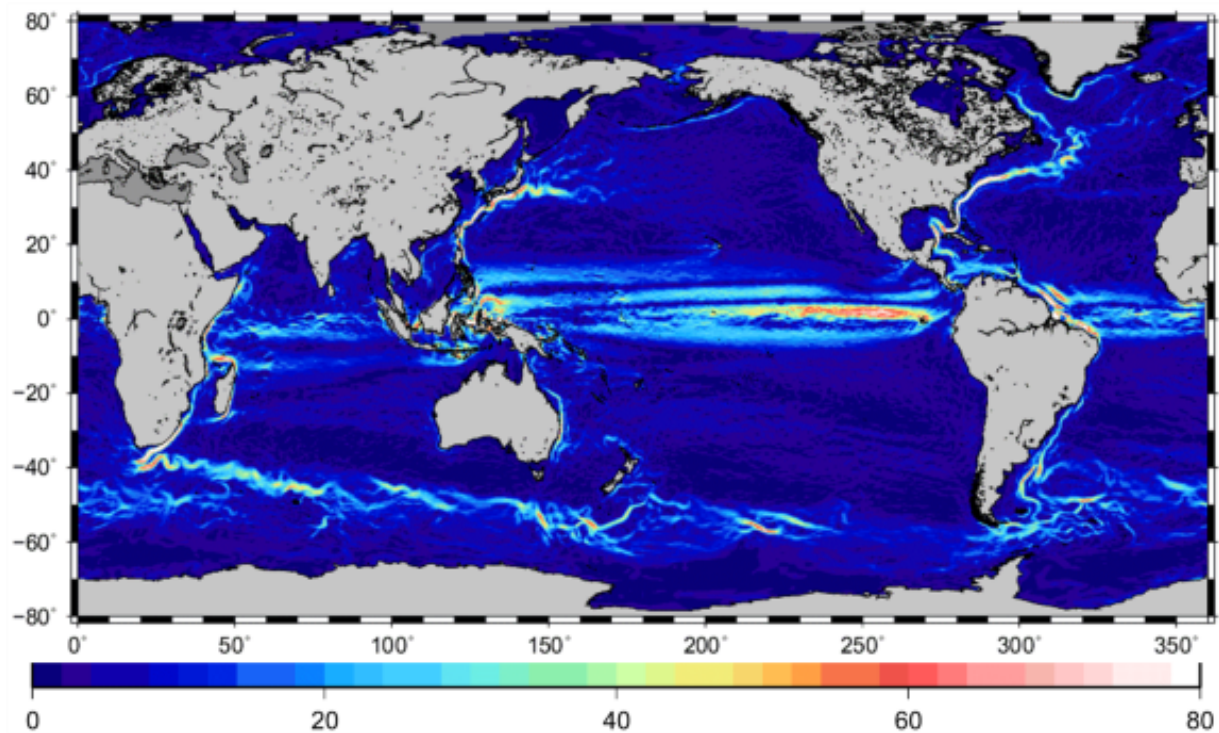


Figure 3a: CNES-CLS13 mean dynamic topography and corresponding geostrophic current averaged over the years 1993 to 2012. Where altimeter observations do not provide estimates of mean geostrophic current, such as along the equator, this information is derived from buoys. CLS15 might be preferable.

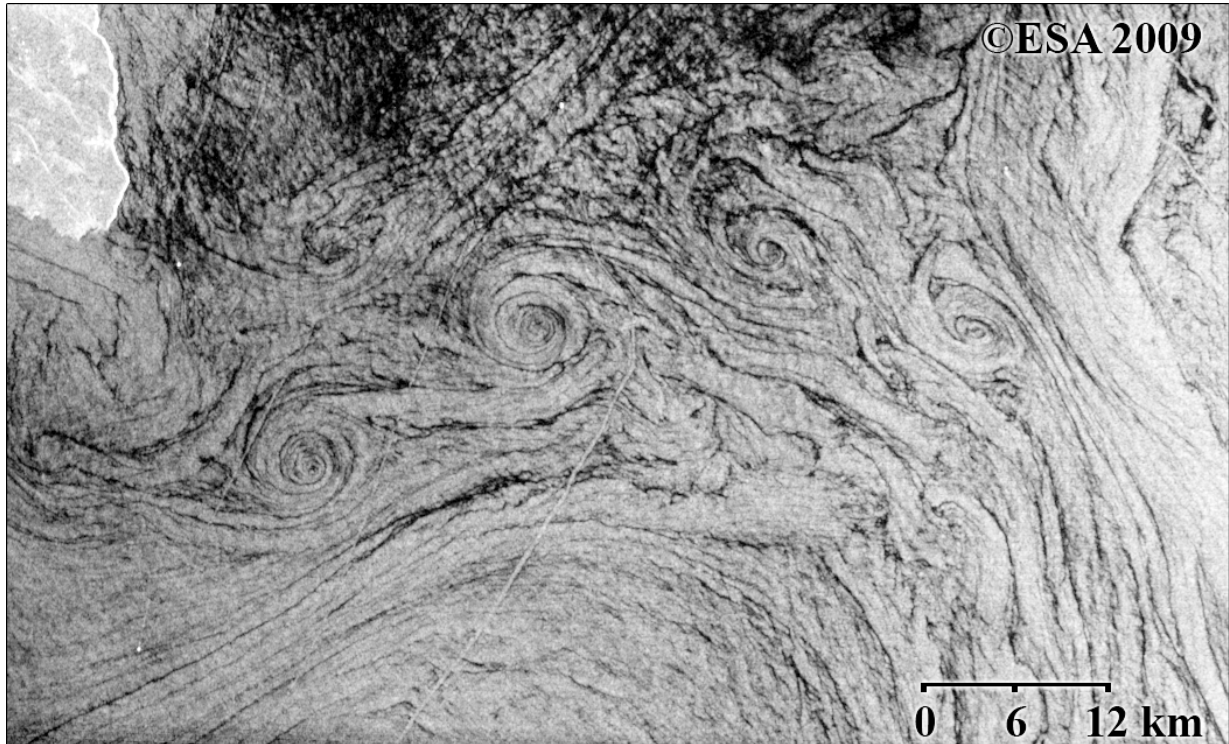


Figure 3b: Spiraling cyclonic eddies at scales around 10 km in the Mediterranean Sea imaged by Envisat ASAR.

This so-called "altimetry gap" has then prompted attempts to combine the lower resolution altimeter data with sequences of medium and higher resolution satellite and in situ observations (see Fig. 4 and Fig. A1.4 in Annex I). A now-common strategy has emerged to derive small-scale tracer structures and so-called Lagrangian coherent structures, from the available large-scale smooth altimetry-derived velocities (e.g., Dencausse et al., 2017). Indeed, using a Lagrangian-dynamical framework, an initial larger-scale tracer field (e.g. sea surface temperature and/or salinity) can be advected on higher-resolution grids, generating much smaller-scale patterns. More specifically, large to moderate straining and vertical motions in the upper ocean can produce filamentary and spiral structures in both active and passive resulting tracer fields.

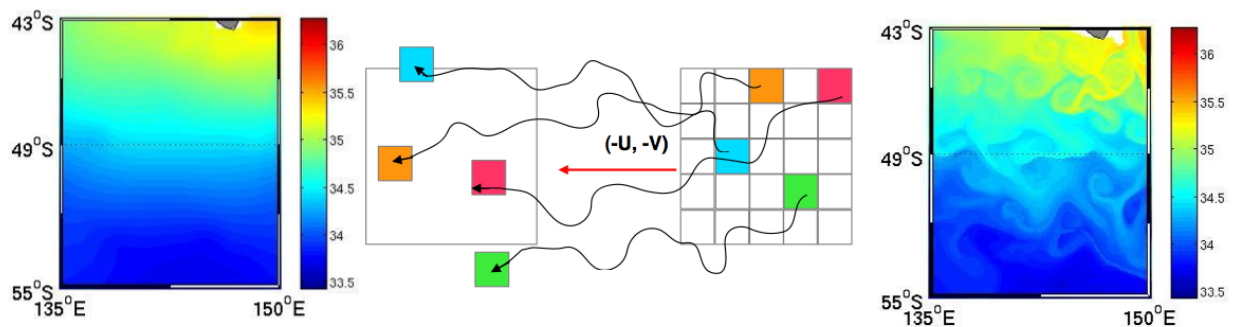


Figure 4: Illustration of the Lagrangian advection to dynamically interpolate large-scale tracer (ARGO surface temperature field, left) onto a high-resolution product (right). Particle trajectories computed using altimetry-derived velocities (AVISO, weekly $1/3^\circ$) with 3 hours time steps [RD-23].

While of considerable use, such a methodology is certainly not sufficient (Berti and Lapeyre, 2014), and the short scale upper ocean dynamics must generally be diagnosed using more

advanced dynamical models. One of them, termed eSQG, for effective surface quasi-geostrophy, can significantly depart from 2-D turbulence. Most importantly, under favorable environmental conditions, eSQG offers major prospects to combine low resolution SSH data and already available medium resolution satellite data, i.e. microwave SST and SSS fields. Novel perspectives include the possibility to retrieve from surface information (such as surface density) not only the surface oceanic current at scales smaller than 100 km, but also the 3-D motions, including the vertical velocity, at these scales in the first 300 m below the surface.

Finally, more direct estimates and/or upper ocean signatures of ocean surface currents and higher-level derived quantities such as frontal boundaries can further be obtained using instantaneous observations, so-called high-resolution snapshots such as frequently demonstrated in the so-called “hotspots-menu” available in the GlobCurrent visualization portal (www.globcurrent.org). In particular, high-resolution optical and/or SAR imaging and Doppler properties can be exploited using an advanced consistent framework. Quite naturally, such a framework can include the analysis of the transformation of surface waves (of different scales) on ocean currents. Indeed, when waves on deep water encounter a spatially varying current, it results in a spatially varying dispersion relation. Accordingly, the phase speed, direction, wavelength, height and even the shape of surface waves can be altered, depending on their wavelength, by the interaction with surface currents.

From a satellite sensor perspective, highly-resolved space-time ocean surface roughness mapping capability can thus be directly exploited to quantitatively infer ocean surface currents and upper ocean deformation field. First, as the relaxation scale of the short scale waves is rather small, from 10 to 100 m (e.g. Kudryavtsev et al., 2005, Rascle et al., 2014, Rascle et al., 2017), spectacular manifestations of mesoscale and submesoscale ocean surface signatures can be quantitatively interpreted. Indeed, under low to moderate wind speeds, high resolution radar and/or optical images (see Figure 5) trace local ocean surface “roughness” anomalies resulting from interactions of short scale wind waves with non uniform surface currents, transformation of the near-surface wind field over large SST gradients, and/or suppression of short waves in surface slicks accumulated by surface current convergences. Among various oceanic phenomena, internal waves (IW) are often reported, to also serve as test beds to assess forward imaging model to advance the quantitative interpretation of high-resolution satellite observations (e.g., Alpers and Hennings, 1984). Compared to optical observations, all-weather radar images can further help to quantitatively separate the measured roughness variations between changes associated with denser breaking patches and purely resonant short-scale scatter modulations. This capability relates to the polarization sensitivity of radar signals (e.g. Kudryavtsev et al., 2013, Kudryavtsev et al., 2014). Polarization decomposition (using co- and cross-polarized high resolution radar signals) efficiently enables the discrimination between surface manifestation of upper ocean dynamics and wind field variability.

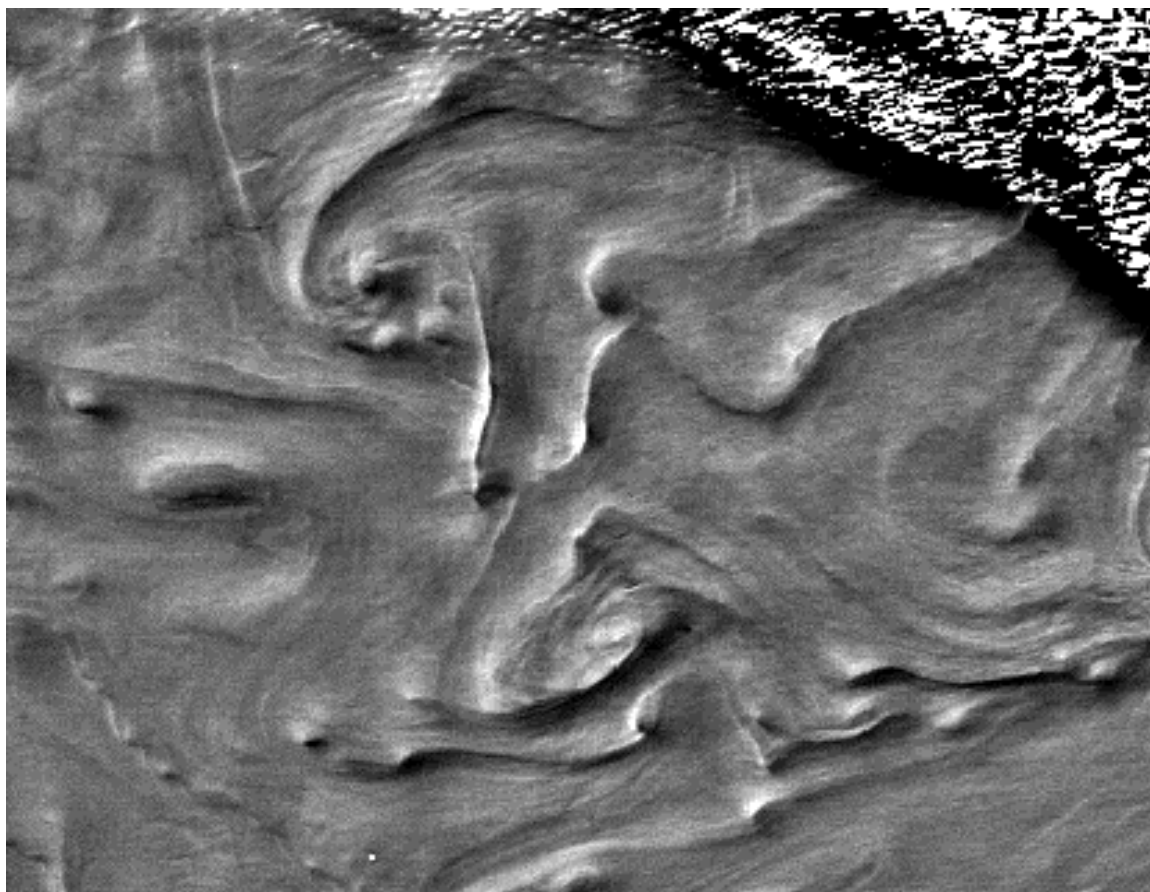


Figure 5: *Surface roughness intense contrasts in the Mediterranean-Libyan Sea from optical sensor measurements in and around the sun glitter area, March 3rd, 2012. Clouds are visible in the upper-right corner. The 900-nm radiance measured by the Medium Resolution Imaging Spectrometer (MERIS), on-board ENVISAT, with resolution of 250 m has been high-pass filtered at 25 km. Resulting surface contrasts evidently trace the upper ocean turbulent state.*

Moreover, Kudryavtsev and co-authors (2017) further unveiled the potential to exploit Sentinel-2 Multi-Spectral Instrument (MSI) specific instrumentation and configuration of multi-channel detectors. Such an overlooked capability can also provide direct means to derive space-time directional and amplitude characteristics of the (imaged) surface waves. In particular, cumulative impact of the current vorticity field on long wave trains kinematics was unambiguously shown to cause significant overall ray deflection. As shown Figure 6, such a principle also applies for swell wave systems detected with SAR measurements, to quantitatively evaluate how the trajectory of wave trains travelling against a strong current can be found to oscillate around the mid-stream, and to then become solely guided by the current (e.g. Figure 6). Based on ray-tracing calculations, and unambiguously revealed from the analysis of Sentinel 1 and 2, the variability of the near-surface current explains significant wave-current refraction, leading to wave-trapping phenomenon and subsequently strong local enhancement of the total wave energy.

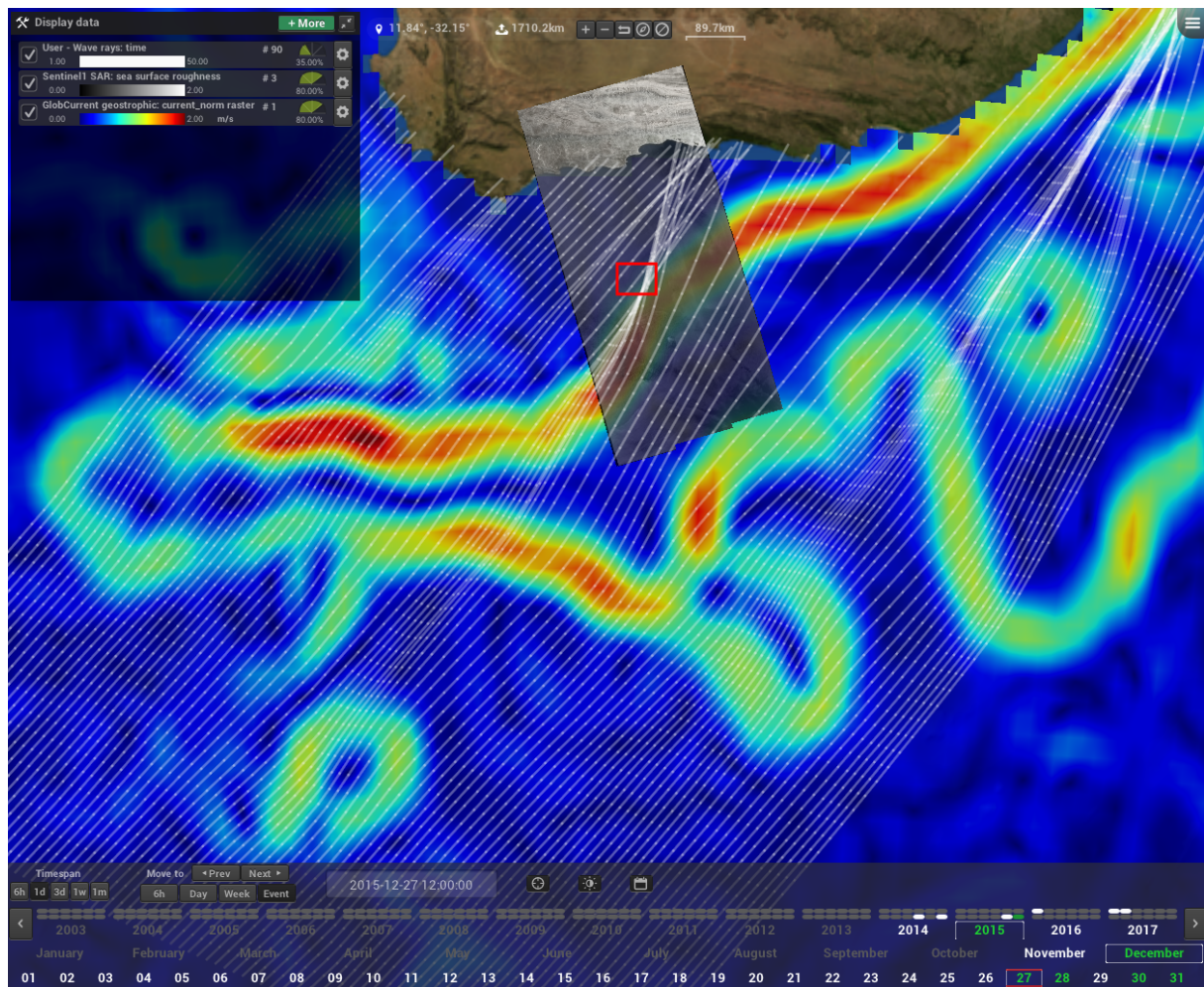


Figure 6: Contemporaneous GlobCurrent geostrophic surface current velocity and Sentinel-1 SAR image on Dec 27, 2015. Rays, white trajectories, are simulating wave propagation path distorted by surface current gradient (e.g. vorticity).

Needless to say increasing in-situ current measurements from drifting and moored buoys, coastal HF-radar installations, Argo floats, gliders and ship observations can also complement the satellite measurements (<https://odl.bzh/goUnQueX>). In particular, drifters have already a long history of use to help mapping large-scale ocean currents, and thus, interpreting satellite sea surface anomaly measurements. Note, surface drifter velocities reflect a mix of ocean currents, wind and wave-induced surface drifts, and direct wind forcing (so-called windage). The latter two components can be strongly sheared in the vertical, and the water-following characteristics of various surface floats can accordingly vary widely. As understood, the very-near surface velocity field is largely controlled by boundary-layer turbulence. To minimize pure surface drift effects, drifters typically include a drogue, to provide velocity estimates at a specific depth beneath the surface (e.g., typically 15 m depth). Particular experimental designs can further be considered to more precisely study the vertical structure of near-surface currents (Kudryavtsev et al., 2008).

Each satellite and in-situ based measurement techniques have thus specific strengths and limitations (e.g., resolution, coverage, accuracy, depth integration, cloud dependence, empirical based retrieval methods, processing limitation, etc). By development and use of systematic data merging and sensor synergy, combined with advanced processing tools and simulation models, the complementary strengths of each sensing technique can be optimized. Deficiencies are thereby reduced and the final surface current estimate is more consistent,

regular and reliable. With near-real time production emerges the opportunity that a much greater provision of services can be supported.

Yet, challenges are numerous. In particular, high-resolution wave-resolved and/or Doppler measurements are not currently globally available. Today, surface current estimation must thus rely upon a different analysis strategy.

Currents that can be observed in the near surface layer of the ocean are composed of different components including: tidal currents, internal wave induced currents, surface wave induced Stokes transport, mesoscale to sub-mesoscale currents, inertial currents and the wind drift as illustrated in Figure 7 and listed in Table 1. Far from the coast and under stationary conditions, the upper layer current is dominated by the last 3 components in addition to the background mean large-scale current. Hence, the geostrophic and (wind-induced) Ekman components, to be derived from altimeter and scatterometer measurements, can therefore be stated to be the key contributions to estimate the total surface currents. Given that the larger ocean geostrophic component generally varies on much slower time scales than motions at smaller spatial scales, estimates of an instantaneous upper-ocean Eulerian velocity field are then interpreted under a 2-scale, coarse temporal (>10 days) framework mostly determined by altimeter sampling. This yield a decomposition between a well resolved smooth component, continuous in time, and shorter-scale, more rapidly uncorrelated in time. Note that in costal regions, tidal current may modify this decomposition.

Relying on this 2-scale framework, Lagerloef and co-authors (1999) first created a surface current model (in the tropical and sub-tropical Pacific basins) derived from satellite altimetry and winds (for the geostrophic and Ekman flows, respectively), with coefficients tuned to match currents derived from available surface drifters. The GlobCurrent products also heavily follow this framework: from statistical regression analysis, an effective wind-induced surface current component is derived to best explain measured differences between altimeter-derived velocities and low-pass filtered drifter currents (e.g. Rio and Fernandez, 2003). The low-pass filter operation is intended to ensure removal of the inertial and higher-frequency motions. As performed, the statistical analysis (regression) provides both the spatial and seasonal variability of these effective Ekman model parameters. The results of this regression corresponds to an effective temporal resolution of about 3 days. GlobCurrent products then generally refer to Eulerian current components at an interpolated spatial resolution of about 30 km and temporal resolution of 1 day (geostrophic current) and 3 hours (so-called Ekman current).

Very near the surface the wave-induced Stokes drift, which has zero Eulerian velocity, further results from the cumulative impact of wave motions, is independently provided, and mostly considered for validation when the trajectories of individual surface drifting buoys are re-analyzed. Note that even surface waves that do not break can further impact the upper ocean. The mean resulting Stokes drift (Figure 7) associated with surface waves can indeed tilt vertical vorticity anomalies into the horizontal, leading to the creation of vortices called Langmuir Cells (LC), often visible as elongated surface convergence patterns (i.e. relic foam lines tracing wind streaks).

As performed, the empirical regression to adjust background geostrophic motions and wind estimates to drifter trajectories may thus possibly include, statistically, a regional and seasonal wave contribution. As designed Surface Velocity Program (SVP) drifters are representative of the motion of a 10 m layer centered at 15 m deep. Undrogued, drifter

trajectories have also been analyzed. Consequently, the targeted reference depths, at which the GlobCurrent products are delivered, are at the surface and at 15 m depth.

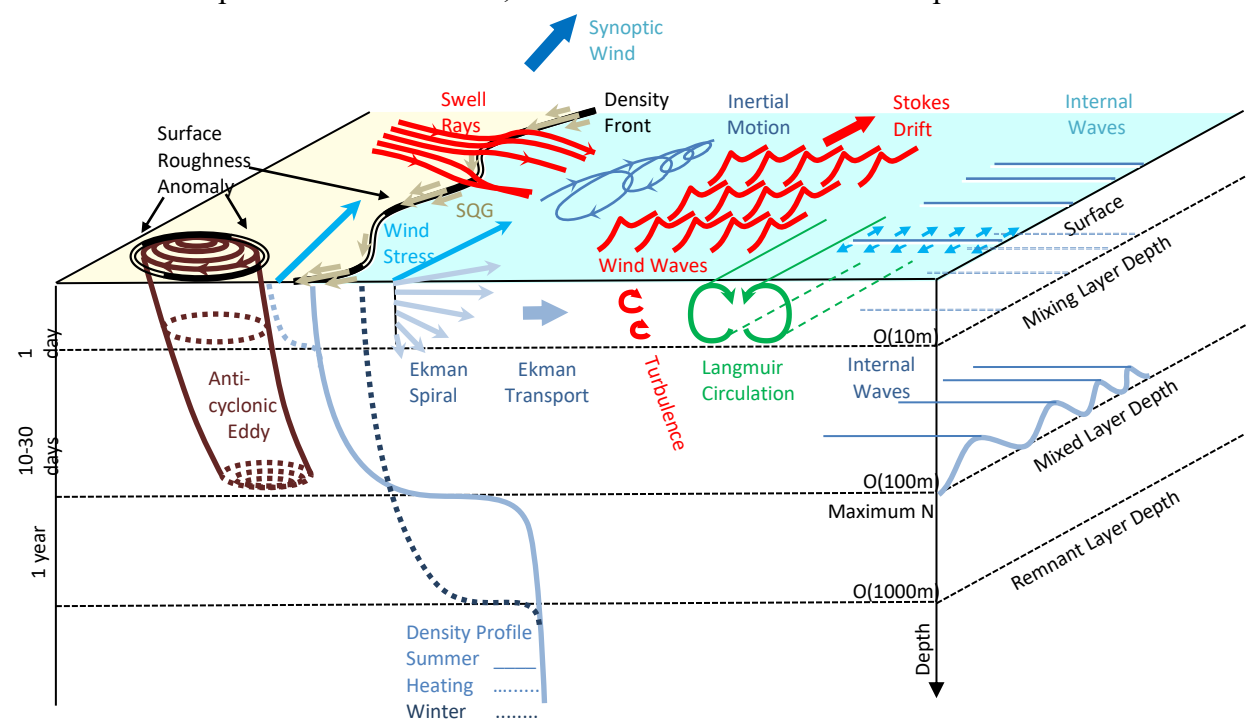


Figure 7: Characteristic features and processes that influence the upper ocean current. Among these are eddies, frontal boundaries, Ekman spiral, Ekman transport, Stokes drift, turbulence, Langmuir circulation, internal waves.

Surface current component	Main measured quantity	Specific sampling requirement	Required ancillary data
Geostrophic current (slow varying)	Sea level anomaly All weather SST/SSS (microwave)	Dual view (from different altimeter orbits) Daily for 25km scales	Geoid and Mean Dynamic Topography at scales < ~100 km
Ageostrophic current	MCC displacements field	Precisely geolocated observations with short separation in time (depend on scales but typically few hours)	
Ekman current	Mean Wind vector	Daily at stationary wind conditions	Mixed layer depth/vertical stratification Geostrophic Current
Inertial current	Wind vector history	3 hourly or better	Geostrophic current, mixed layer depth/vertical stratification, surface drifter data at 1 hour

			temporal resolution
Stokes drift	Directional wave spectrum	3 hourly or better	
Tidal current	Doppler shift (HF radar grazing angle)	Hourly or better	
Total surface current (TSCV)	Doppler shift/ATI phase	Dual view	
TSCV rotational	Wave phase velocity excess from cross spectra analysis, from dual optical channel or SAR multi-looks Spatial variations of peak wave direction and wavelength	Dual channels or looks must have optimal time separation	Wind wave spectrum
Strain	MSS variations	Hourly or better	Wind vector

Table 1. Surface current types observed in the near surface layer and their corresponding measured quantities, sampling requirement and requirement for auxiliary information.

3. Ocean Current Terminology and Symbology

In this section the ocean surface currents are classified and identified according to different phenomena (Table 2) and types (Table 3). Among the important forces acting on the ocean are:

- Large scale (> 10 km) forces due to variations in surface elevation (gravitation, including tides, atmospheric pressure, local topography).
- Friction from the wind.
- Ocean surface wave-induced transport through non-zero Stokes drift.
- Coriolis force related to the Earth rotation. Ω is the magnitude of the Earth's rotation vector.
- Forces due to variation in density, and effect on stratification. Stratification of the ocean refers to its density separation into layers owing to the dependence of the density on temperature, salinity and pressure. The rate of density change is related to the Brunt-Väisälä frequency $N = \left[-\frac{g}{\rho_0} \partial \rho / \partial z - g^2 / c^2 \right]^{1/2}$, c the speed of sound. Note also that a slippery near-surface layer can develop due to intense daytime solar heating [RD-14].

These forces lead to the development and co-existing of different flows and phenomena (see Table 2), and are usually described as:

- Geostrophic motions (due to the horizontal pressure gradient force, balanced by the Coriolis force). This corresponds to a particular simplification of the equations governing the horizontal components of velocity. It is valid when the largest terms in the equations of motion reduce to the Coriolis force and the pressure gradient. This can generally apply in the deep ocean over large (> 30 - 100 km) spatial and long (> 3 - 10 days) temporal scales. These motions encompass:
 - Barotropic motions: Driven by the slope of the water surface causing a

horizontal pressure gradient. The barotropic currents are not varying with depth.



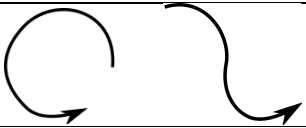
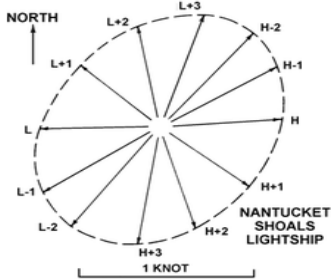
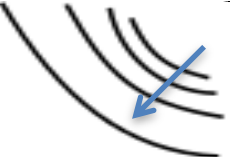

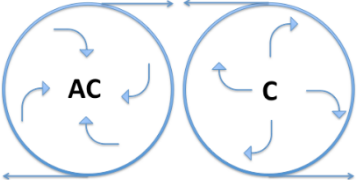
- Baroclinic motions: Driven by vertical variations in the density of the water. Pressure and density levels are not coincident. The baroclinic currents are varying with depth.
- Inertial motion: the motion continues without friction as a consequence of an initial set-up (momentum). Due to the Coriolis force, inertial motions are quasi-circular.
- Wind and wave driven motion in the upper layer: frictional motions induced by the wind stress and wave-induced Lagrangian advection (Stokes drift). The wind stress is often parameterized as a function of the square of the wind speed and a drag coefficient. The Stokes drift is usually derived as the mean velocity of the slopes of the surface waves. Vortex forces in the upper layer leading to Langmuir circulation can emerge from the interaction between the wind- and wave induced motions.
- Internal waves: waves to occur at the boundary between water layers of different densities.
- Tidal motion (horizontal and internal waves of tidal period), related to gravitational variations associated to the Sun and Moon alignments, resulting in periodical changes in water levels.
- Kelvin waves: coastal-trapped waves generated by a tidal wave or a storm surge.
- Inertial gravity wave response resulting from a bursting extreme wind event moving in the open ocean.
- Rossby waves: waves, associated to zonal flow, generated to conserve the potential vorticity (rotational momentum).
- Gravitational-gyroscopic waves: internal waves of sufficiently long period, associated to wind stress and/or atmospheric changes/bursts, for which the Coriolis effect becomes important.

Considering U and L , typical velocity and length scales of the motion, the trajectory of fluid parcel will start to be influenced by the ambient rotation if $\epsilon = \frac{2\pi/\Omega}{L/U}$ is on the order or less than unity. Given Ω the magnitude of the Earth's rotation vector, rotation effects are important for $U \leq L * 1e^{-5}$, such as 1 m/s for 100 km scale. To note, surface waves, crossing entire ocean basins, are not affected by Coriolis effect, but can possibly be strongly refracted by ocean currents. The typical number to compare horizontal advection and Coriolis force has been defined as $\frac{U}{L\Omega}$, the so-called Rossby number.

Typical phenomena	Length Scale L	Velocity scale U	Time scale T	Vertical scale H
Orbital motion of surface waves	Basin scale	0 - 2m/s	Hours to weeks	O(10 m)
Wind driven motion	10 - 1000 km	0 – 0.5 m/s	Hours to weeks	O(10 m)
Stokes Drift	10 - 1000 km	0 – 0.5 m/s	Hours to week	O(1m)
Langmuir circulation	10-30 km	0 – 0.5 m/s	Hours	O(10 m)
Internal waves	1-20 km	0.05-2.5 m/s	Hours to days	O(100 m)
Major surface geostrophic currents	30-500 km	0.1-2.5 m/s	3 days to seasons	O(100 m)
Large eddies, fronts	10-300 km	0.1-2.5 m/s	Days to weeks	O(100 m)
Coastal upwelling	1-20 km	0.1-0.5 m/s	Several days	O(100 m)
Tidal currents	1-500 km	0-5 m/s	Hourly	Bottom

Inertial currents	1-50 km	0-0.3 m/s	3 hourly	O(10 m)
Kelvin waves <ul style="list-style-type: none"> - coastal trapped - equatorial trapped 	~ 30 km ~ 250 km	~ 2 m/s 2.8 m/s	Daily to weekly Monthly to seasonal	Bottom
Inertial gravity wave response	10 - 100 km	~ 1- 2 m/s	1-10 days	O(100 m)
Rossby waves	> 200 km	0.05 – 0.2 m/s	Monthly to seasonal	O(1000 m)

Table2: Ocean current classification.

Type	Symbol	Direction	Magnitude
Streamlines		Isolines of the surface height corresponding to the direction between 2 points. Could also indicate the filament structures of chlorophyll concentration	In the gradient of the isolines. Signals the combined effects of horizontal transport and vertical motion
Arrow		Vector that marks the flow direction connected with individual components of the current	Length of the arrow
Trajectory		Eddy, meander, spiral and frontal direction given by the arrow	Eventually given by the trajectory width
Tidal ellipse		Direction from the center, length related to the directional occurrence	Given by the elliptical shape
Internal wave surface signature		Direction from the main front orthogonal	Wave-packet from which the wavelength is given by the separation between the wave-fronts
Oceanic Fronts		Feature that separates two distinct water masses (temperature salinity, roughness)	Strength is related to the gradient. Cold/warm side of the fronts can be marked with blue/red symbols.
Isolated Eddies		Anticyclones (AC) rotate clockwise (northern hemisphere). Cyclones rotates anticlockwise (northern hemisphere)	Magnitude of the sea level anomaly, the Rossby radius of deformation and the orbital velocity. AC lifts the pycnocline in the center. Cyclones suppress the pycnocline in the center.

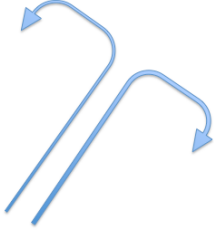
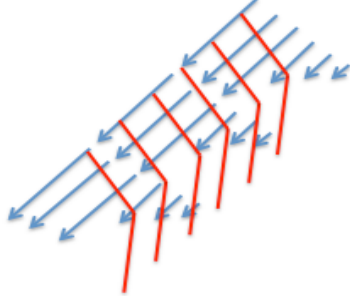
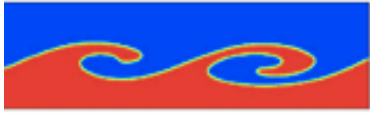
Mushroom or hammer-head		Direction illustrates the existence of an anticyclone and a cyclone originating from mesoscale frontogenesis.	
Wave-Current refraction		The wave-current interaction induces a bending of the wave front that in turn cause a change in propagation direction. Simultaneously the wave height and length (wave spectra) undergo changes.	Curvature of the bending.
Spirals on the sea		The Kelvin–Helmholtz instability can occur when there is velocity shear in a single continuous fluid, or where there is a velocity difference across the interface between two fluids.	Intensity is related to the strength of the shear

Table 3: Ocean current symbology.

Strong ocean currents are generally confined to the upper hundred meters of the water column, but can extend over very large horizontal scales (> 100 km). Correspondingly, considering that the volume is a good proxy for mass, the vertical velocity must be constrained, and much smaller than typical horizontal velocities. Large-scale flows can thus be termed as relatively shallow $H \ll L$, H vertical length scale, and almost bi-dimensional $W \ll U$, where U and W are the horizontal and vertical velocity scale.

Yet, at a given location, motions distributed over the vertical continuously modify the fluid density. To evaluate the importance of stratification, the comparative ratio between potential and kinetic energies is constructed as $\frac{g\partial\rho H}{\rho_0 U^2}$, a Richardson number, with ρ_0 the density, $\partial\rho$, the vertical density variation across the height scale H . If the ratio is large, there is insufficient kinetic energy to significantly perturb the stratification. If the ratio is small, on the other hand, potential energy modifications can occur, and stratification hardly affects the flow. This process can lead to intense vertical mixing and erosion. When the ratio is on the order of unity, stratification is again important, as an equivalent portion of kinetic energy must compensate a typical potential energy increase.

To note that when rotation and stratification effects are both important (commonly defined by the Rossby radius of deformation), preferential length scales can be evaluated over which typical motion will take place. As observed and evaluated (with satellite altimetry), most of the total kinetic energy (about 80 %) is governed by meso-scale eddies of about 50-200 km, lasting 10-300 days, the so-called building blocks of the ocean « weather ». Such mesoscale energy is manifested as mid-ocean eddies and as boundary current variations that develop from meanders to eddies and rings. Identified forms that can be regularly observed from high-resolution satellite measurements (e.g; Fig. 3) and include chains of eddies, individual spiral eddy, and mushroom-shaped flows.

4. Upper Ocean Currents

The upper oceanic surface velocity field is strongly influenced by the forcing acting at the air-sea interface. As such, the upper ocean involves a continuum of variability across all space and time scales, to become subject to small- and large-scale random perturbations and interactions. The water on the continental shelf is mostly moved by the tides and coastal currents, and often stirred throughout its depth by the wind stress at the surface. In the deeper open ocean, on the other hand, the vertical structure of the water masses is generally characterized by the presence of large temperature gradients within the upper few hundred meters. In this upper ocean, inter-related motions co-exist to govern the energy and momentum exchanges between the atmosphere and the underlying deep ocean. In particular, the wind-generated surface waves (SWs) influence the momentum and energy transport from the atmospheric boundary layer via the ocean surface to the upper ocean. Most losses of the SW energy directly contribute to the generation of small-scale turbulence, whereas momentum losses more directly induce upper ocean drift currents.

Surface Forcing: Indeed, when the wind blows over the surface, a tangential stress develops to generate surface drift in the upper homogeneous layer of the ocean. As often stated, the transfer of momentum and energy across the air-sea interface provide the sources of almost all oceanic motions. Furthermore, the horizontal length scales of the mean properties of these motions are almost always much greater than their corresponding vertical scales as indicated in Table 2. Considering a situation for which the wind has blown steadily over a large area for a time long compared with $1/\Omega$, Ω being the magnitude of the Earth's rotation vector, the wind stress is almost entirely transmitted locally to the underlying water. A velocity scale, w_* for the water motion can then be approximated as $w_* \sim (\tau_0/\rho_w)^{1/2}$, where τ_0 is the wind stress and ρ_w the water density. When the wind exhibits long-range temporal correlations, the surface waves are in equilibrium with feedback on the surface wind stress, also leading to a combined Stokes and surface drift.

Within the depth range $|z| \ll w_*/\Omega$, the Coriolis effect is negligible, and the stress and buoyancy flux are approximately constant and determined by the external surface conditions. When the density of the fluid is quite uniform, the local velocity gradient reduces to the form $\frac{\partial u}{\partial z} = \frac{w_*}{\kappa z}$, where $\kappa = 0.42$, leading to a standard logarithm profile. The present understanding of links between waves, turbulence, and surface shear currents is still an active scientific research area. Yet, a commonly accepted model is to consider the existence of a “wall” turbulent boundary layer beneath the surface.

As mentioned above, the same surface wind that causes the turbulent layer also causes surface gravity waves, either in local equilibrium with the wind or in disequilibrium due to a transient history or remote propagation as for swell. As commonly experienced, within the oceanic surface top layer, the predominant motions can generally be attributed to the gravity waves. The thickness of the active upper layer is then determined by the turbulent intensity of the short scale breaking waves carried by the orbital velocities of the larger dominant waves. Moreover, it has for long been recognized that these large gravity waves transport mass and momentum. Both are related to the difference between the average velocity of a fluid parcel (Lagrangian velocity) and the current measured at a fixed point (Eulerian velocity). This difference, first identified by Stokes (1847), is called the Stokes drift (Figure 8). For a statistically stationary and horizontally homogeneous wave field, the total surface wave drift is well approximated as the sum of the drifts of the individual wave components, distributed as

$$U_s(z) = \iint 2\omega k S(\omega, k) e^{2|k|z} dk d\omega, \quad [1]$$

with $S(\omega, k)$ being the directional wave energy spectrum.

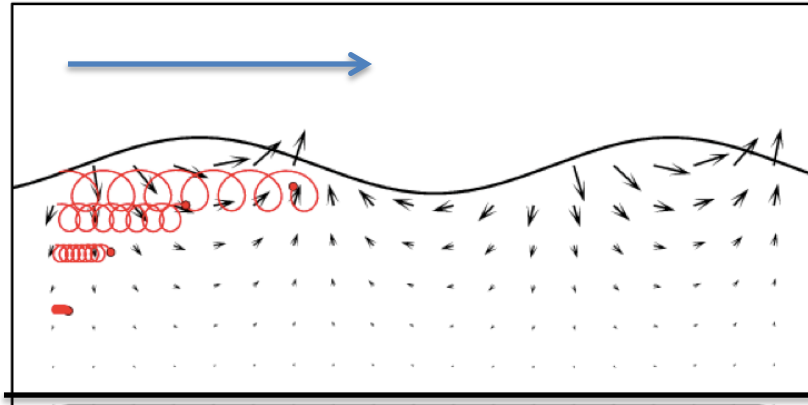


Figure 8. Schematic illustration of the Stokes drift and Stokes depth. The blue arrow indicates the wave propagation direction. The black arrows are instantaneous vectors marking the strength of the orbital motion of individual particles (at the surface and at different depths) induced by the propagating wave. The red loops indicate the total horizontal distance that the particles have moved over the course of 7 passing waves.

As defined, the Stokes drift decays relatively rapidly away from the surface, over a length scale, known as the Stokes depth (Figure 8). For random waves in equilibrium with the local wind, the depth where the Stokes drift is truly significant is generally well approximated by the wind sea significant wave height, $H_{sw} \approx 0.02 U_{10}^2$, with U_{10} the wind speed at 10 m. Accordingly, for a 10 m/s wind speed, the Stokes depth is about 2 m. Moreover, near the surface, the surface Stokes drift induced by the waves typically accounts for 1/2 of the total surface wind-induced drift. In presence of an upper layer drift, an instability mechanism can arise from the possible tilting of vertical vortices, associated to infinitesimal downwind surface jets, by the Stokes drift of the surface waves. The vortices have opposite signs on the two sides of the jets, and this instability mechanism can then produce longitudinal rolls, with the surface convergence at the jets, known as Langmuir patterns (see Figure 9).

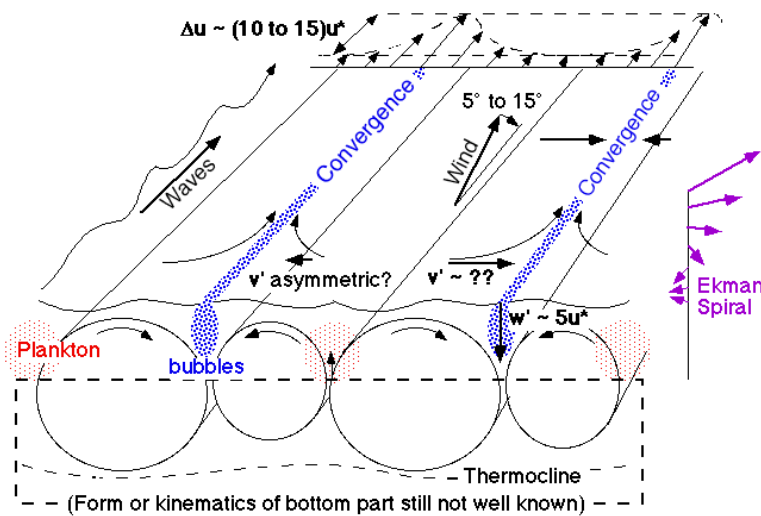


Figure 9. Schematic illustration of the Langmuir circulation (first described by Langmuir, 1938). The separation scale of the convergence zones are typically 10-100 m. Courtesy Jerome Smith.

Ekman Current: When the depth increases, the Coriolis effect becomes important, and the direction and magnitude of the mean velocity will further vary with depth. Following the mean momentum equation, the net transport in the surface layer can be derived, leading to the infamous Ekman transport. In its canonical derivation, the transport is independent of the stratification, and is found oscillatory with time with the inertial frequency, $f = \Omega \sin \lambda$, λ the latitude. Its magnitude and direction depend on the time history of the wind stress $\tau = \rho_w w_*^2$. If a mean transport, averaged over many days, is considered, the steady Ekman transport is normal to the wind stress, towards the right (left) in the northern (southern) hemisphere, with magnitude τ/f .

Consequently, the shear current near the upper wavy layer is expected to evolve with depth following a logarithmic profile and a further rightward (leftward) spiral, as sketched in Figure 10.

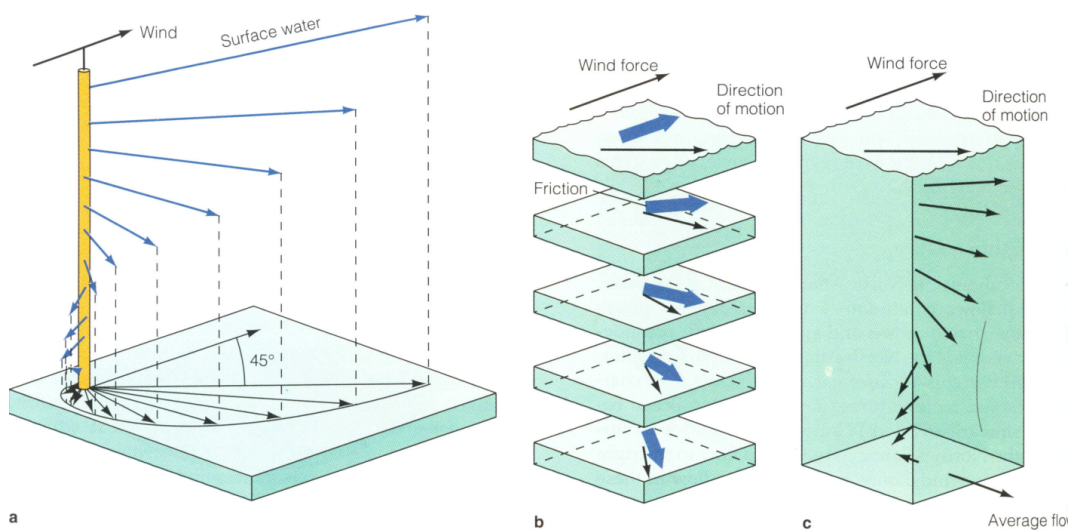


Figure 10: Current profile in the upper layer induced by the Ekman spiral.

Considering the influence of surface gravity waves, a modification of the Coriolis force must be considered through the inclusion of the Stokes drift profile $U_s(z)$ acting as a “vortex force” to possibly modify the classical Ekman spiral model. Accordingly, the vertical profile of the quasi-Eulerian current, its magnitude and surface angle, will depart from the classical model of Ekman (1905). In particular, the surface angle could be much larger than the standard 45° direction to accommodate for the strongly directional and sheared $U_s(z)$, as illustrated in Figure 11 (from [RD-12]). Here, radar HF measured vector, U_R , has been interpreted as a sum of a quasi-Eulerian current, U_E , representative of the upper 2 m and a filtered surface Stokes drift, U_{sf} , taking into account a nonlinear wave correction. The full surface Stokes drift is typically 40% larger than this filtered value estimated to be on the order 0.5-1.3 % of the wind speed. As reported, the quasi-Eulerian current, U_E is then of the order 0.6 % of the wind speed, and lies at an average between 40° and 70° , to the right of the wind direction (Northern hemisphere).

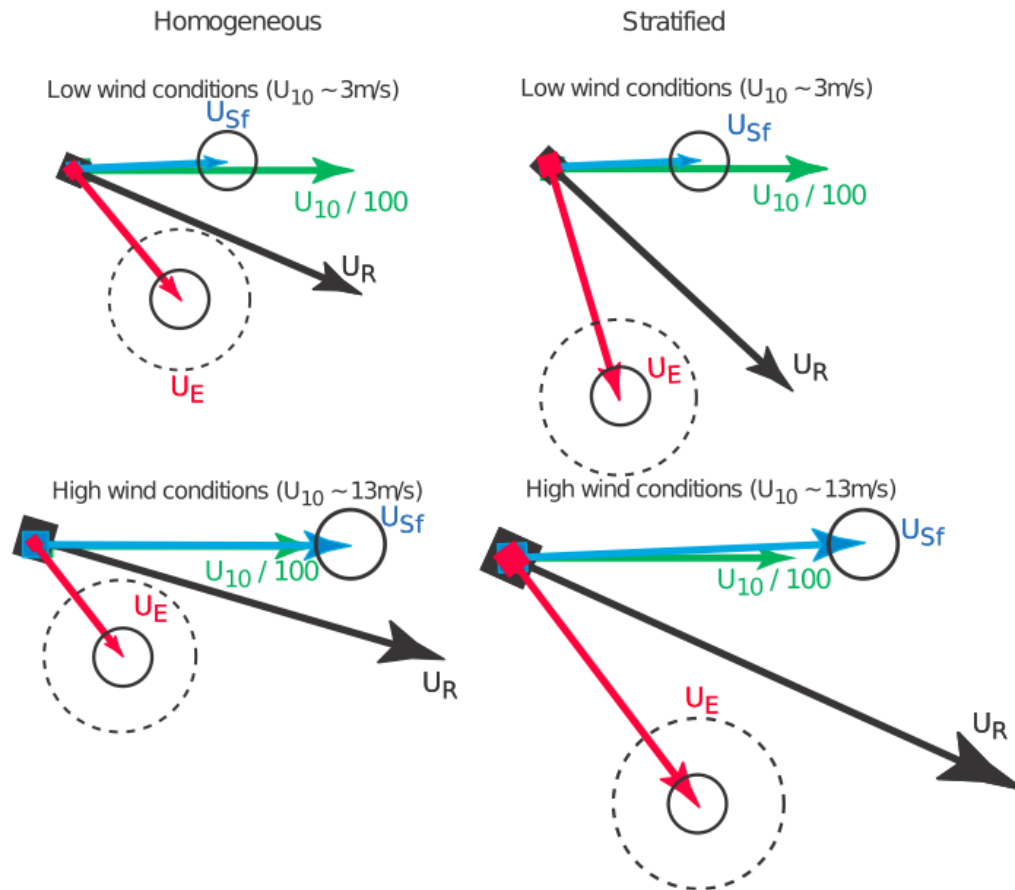


Figure 11: Modification of the classical Ekman induced current spiral by Stokes drift. Circles indicate uncertainties.

As generally observed, the wind-wave driven current is then not expected to be significant for depths $|z| \geq w_*/\Omega$. Typically, for a 10 m/s wind speed, this Ekman depth is of the order of 10-30 m. This depth of maximum influence can further be limited by the vertical stratification and the buoyancy effect [RD-13], leading to larger velocities in shallow upper mixed layers, with directions more strongly deflected to the right (Northern hemisphere).

Geostrophic Current: Moreover, the Ekman transport must be understood to be relative to and superimposed on the mean motion of the underlying water. In the open ocean, this mean motion is considered to be approximately geostrophic (see Figure 3a) and associated with small departures from a level of no motion, at great depth at which horizontal pressure gradients, Reynolds stresses and mean motion all vanish. Accordingly, the mean momentum equation can be integrated to this depth. This leads to the Sverdrup transport equation to relate the sum of the Ekman and Sverdrup transports to the wind stress curl. In cases in which the geostrophic flow is strong enough, the geostrophic vorticity can then affect both the decay scale and oscillatory variation in the Ekman layer. To leading order, the total vorticity can be estimated as the sum of Coriolis and local geostrophic flow.

Inertial Current: As discussed, among key processes, the distribution of purely wind-driven ocean currents will strongly depend on the temporal correlations of the forcing wind and resulting waves. Importantly, when the wind and the wave forces that have set the upper ocean into motions cease, the water will not rest immediately. Energy imparted by the wind and waves takes time to fully dissipate. The Coriolis force will then continue to apply as a centripetal force, leading to rotational flows, referred to as inertial currents, as shown in Figure 12. The period of the rotation will vary with the local Coriolis parameter (e.g. latitude

dependent). The effect of pre-existing organized currents, such as those due to an eddy, can shift the oscillation frequency, correcting the Coriolis frequency with the vorticity of the underlying motion.

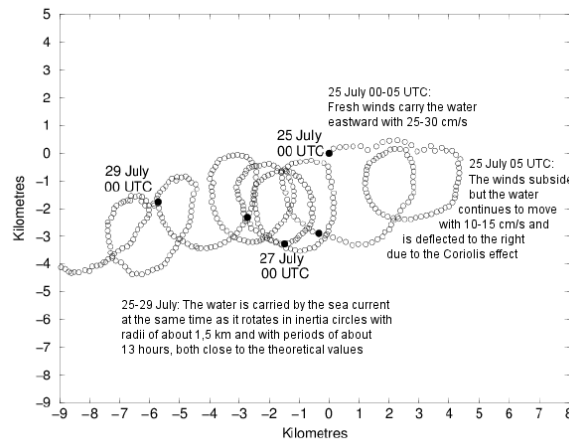


Figure 12. Looping trajectory of surface buoy illustrating the effect of the inertial motion following the decay of the wind forcing. Note that the surface drifter data¹¹ has recently been released with hourly temporal resolution ensuring proper sampling of the inertial motion (Lumpkin personal communication at UCM-3, March 2017).

Not to be neglected, moving patterns of wind stress, such as tropical cyclones and hurricanes, can also generate internal waves (IWs). Indeed, as divergent surface wind distributions induce vertical motions, some resonance can occur. Moreover, when surface waves propagate across the ocean surface, they often form series of wave groups. If the group velocity of the surface waves matches the phase velocity of an internal wave, resonant energy exchanges can thus also occur. The rate of energy transferred to internal waves is certainly much smaller than to surface waves, but the wave amplitude for a given energy density is larger by a factor $\rho_0/\partial\rho$, where $\partial\rho > 0$ is the difference in density across the pycnocline. The surface waves can then further be modulated in the field of orbital velocities of the internal waves. Feedback mechanisms will then contribute to modulate the internal wave field and, in interaction with the drift currents, the generation of upper ocean currents can be altered. Furthermore, these interactions, generated by fast changes of the wave and wind stress vectors, play an important role in setting the surface mixed-layer depth (e.g., fast extreme high wind events).

Finally in the case of low wind speeds, large diurnal warming or strong rainfall will contribute to increase the static stability of the upper ocean. In turn, the buoyancy fluxes become the dominant processes to suppress the turbulent exchange with deeper waters. In result, the turbulent mixing is then mainly localized within a more stably stratified near-surface layer that can slide over the underlying water with a minimum friction. This slipperiness can lead to surface velocities significantly larger than those observed in a well-mixed standard Ekman layer. In these special “extreme cases”, the general vertical profile model will not provide reliable surface velocities, and a slippery layer model should preferably be considered.

¹ Satellite-tracked drifters now provide a large homogeneous data set of global near-surface current observations. As developed [RD-23], these observations can be decomposed to derive the global distribution of time-mean near-surface ocean currents, but also their seasonal cycle, and the variance of eddy fluctuations. The drifters have a drogue centered at a depth of 15 m to reduce the downwind slip to $\sim 0.1\%$ of the wind speed for winds up to 10 m/s, to follow the water within the mixed layer. When this drogue is lost, the downwind slip largely increases to $\sim 1\text{--}1.5\%$ of the wind speed. The spatial mapping is reaching $0.5^\circ \times 0.5^\circ$, using data within ellipses set from the variance of eddy fluctuations, evaluated from the data and starting with $2^\circ \times 2^\circ$ bins.

Ocean Surface Currents (OSC) must thus be considered as the cumulative results of numerous local and remote factors as expressed in Table 1, including highly variable winds, surface and internal waves, tides, mixed layer depth and buoyancy fluxes. Interacting with larger scale flows, the influence of these random forces on OSC is not trivial, and understanding the interplays between dispersion and confinement is essential for fluid transport processes as well as mixed layer dynamics (e.g. [RD-16], [RD-21]).

Yet, as now revealed, well-ordered and long-lived coherent mesoscale structures often emerge, with horizontal scales of 30-300 km, and with time scales of 3-30 days. These are the spatial and temporal scales that define the GlobCurrent global and regional (Mediterranean Sea) products. Moreover, instantaneous snapshot products, including SST gradients, sun-glitter, SAR roughness anomalies, can further be quantified to evidence the rich the upper ocean dynamics. All in all as illustrated in Figure 13 this forms the analysis and interpretation framework that has been developed and applied in the GlobCurrent project.

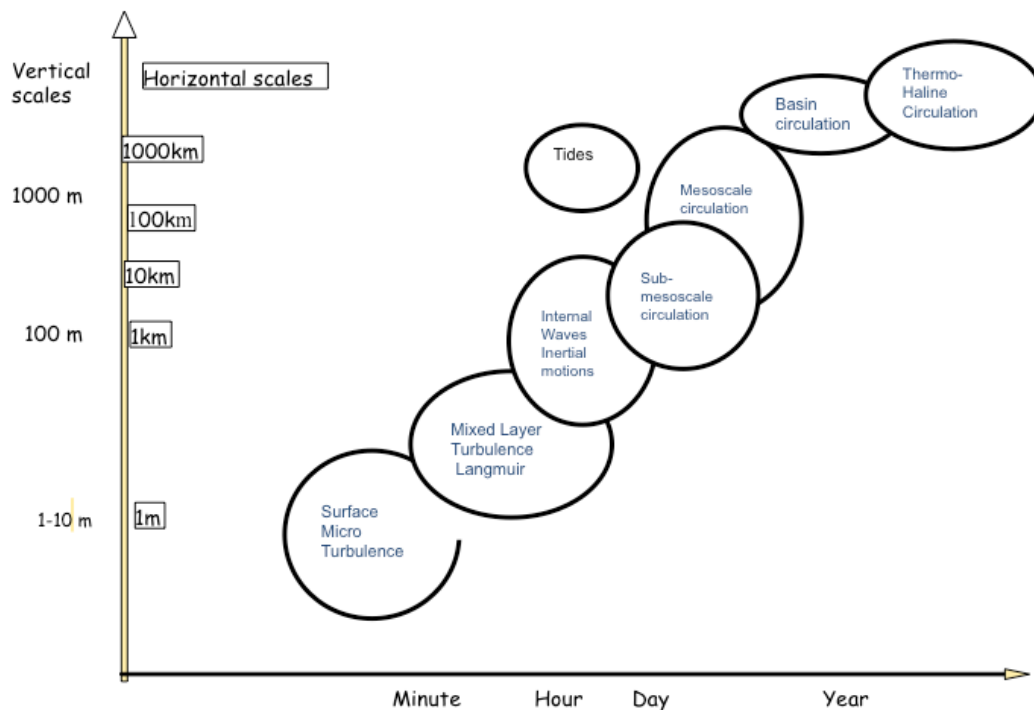


Figure 13: Typical horizontal and vertical scales of key ocean surface current features related to corresponding time scales.

5. Ocean Surface Current Interpretation Framework

As intended, the interpretation framework discusses some governing equations and relationships to help interpret the practical (available) solutions applied to derive the upper ocean surface currents. Among existing products, global estimates are OSCAR (Bonjean and Lagerloef, 2002), SURCOUF (Larnicol et al., 2006), GEKCO (Sudre and Morrow, 2008), SCUD (Maximenko and Hafner, 2010), and now GlobCurrent (<http://globcurrent.ifremer.fr/products-data/data-catalogue>; Rio et al., 2014). In practice, these solutions heavily build on a 2-scale, coarse temporal, framework: a decomposition between a well resolved, large scale, smooth component, continuous in time, and a small-scale component, more rapidly uncorrelated in time as shown in Figure 13. Accurate knowledge of

the ocean's mean dynamic topography (MDT) has been constantly refined, thanks to more accurate gravity field and geoid information together with altimetry and in-situ observations (e.g. Rio et al., 2014).

Satellite altimetry measurements are then used to estimate sea surface height anomalies, added to the MDT estimate, to constrain large and slow evolving components of geostrophic velocities. Note that estimates become singular near the equator, where the Coriolis parameter tends toward zero. In the equatorial band, a Beta-plane approximation is then used, and geostrophic velocities become proportional to the second derivative of the SSH. Altimeter-based SSH maps are representative of about 10-days and 100 km. These medium resolution components of geostrophic velocities are then subtracted from drifter velocities (surface and the 15m depth) whereby the residual velocities are obtained at two different depths. As constructed, these residual velocities correspond to more rapidly time-varying components, including small-scale geostrophic components and wind-wave-induced ageostrophic contributions. To best remove inertial and higher-frequency motions, the residual current estimates are further filtered in time (~ 3 days), taking into account the local inertial period. To simplify, this residual upper surface current, as function of the depth, is then expressed as

$$\vec{U}_{residual}(z, lat, lon, time) = F(z, lat, lon, time, \vec{\tau}, \dots) e^{i\theta(z, lat, lon, time, \vec{\tau}, \dots)} \quad [2]$$

where $F(z, \vec{\tau}, \dots)$ and $\theta(z, \vec{\tau}, \dots)$ are then to be determined. To first order, these functions are local with seasonal variations and strongly depend on $\vec{\tau}$, representing the time and spatially averaged (wind-wave dependent) tangential stress. While not explicit in this expression, contributions from waves, underlying meso- and sub-mesoscale flows, as well as unresolved delta-correlated in time processes (wind and wave changes during the time-average operation), certainly modulate the F and θ functions.

A reliable estimation of the Stokes drift (see equation 1) using a numerical wave model is now recognized to be essential for a more accurate interpretation of the near-surface drifter measurements. The largest and steepest waves support the Stokes drift, and define a depth of maximum influence proportional to the wind sea significant wave height. This roughly scales with the wind speed as, $H_{sw} \approx .02 U_{10}^2$. At this depth, the resulting quasi-Eulerian current (considered as representative of the upper 2 m) is certainly strongly reduced. The exact thickness of the active upper layer could possibly be more precisely determined by considering the turbulent intensity of the short scale breaking waves, carried by the orbital velocities of the larger dominant waves. To ease the definition, the reference depth for the uppermost layer OSC product shall scale with this wind sea significant wave height. For low wind speeds ($< 4-5$ m/s), the reference depth will thus correspond to the upper 30-50 cm layer.

With stronger wind blowing on the ocean's surface, waves with breaking events will appear, and can strongly dominate the injection of kinetic energy into the upper ocean. Whether this kinetic energy goes into accelerating the drift or into turbulence will crucially depend on the ambient density and underlying stratification. As also previously discussed, research in the last few decades identified the importance of Langmuir circulations to enhance mixing and turbulence in the upper ocean. Under most environmental conditions, the influence of surface gravity waves have then been postulated to become significant to affect the Ekman layer. Consequently, the Stokes-Coriolis and vortex forces are the main processes to impact the proper determination of upper ocean drifts. Yet, considering a simplified framework, these wave-induced impacts are not distinguished from an overall effective upper ocean forcing, $\vec{\tau}$.

Below this uppermost wave-layer depth, it is then usual to consider the canonical solution for the horizontal momentum equation expressed in the form $u_t - fv = -P_x/\rho_w + (Au_z)_z$, and $v_t + fu = -P_y/\rho_w + (Av_z)_z$ with $(u = u^e + u_g, v = v^e + v_g)$, the sum of geostrophic and ageostrophic velocities in the upper ocean layer, with P the surface pressure associated with the large-scale circulation. In this simplified model formulation, A is characterizing non-linear terms in the momentum equations after applying a Reynolds decomposition. The surface boundary conditions are then $(Au_z^e)_{z=0} = \tau_x/\rho_w$ and $(Av_z^e)_{z=0} = \tau_y/\rho_w = w_*^2$, $\vec{\tau}$ the spatially averaged tangential stress, with w_* the friction velocity in the water related to the overall upper ocean forcing, considering the limit $(u, v) \rightarrow (u_g, v_g)$, at large depth. This lower limit can be interpreted as the base of the Ekman layer.

The thickness of the upper stress-driven boundary layer is then usually expressed as $\delta = (\mu_t/f)^{1/2}$, where $\mu_t \sim 2A$ is a turbulent eddy viscosity parameter. Following similarity between the oceanic and atmospheric boundary layers, the turbulent eddy viscosity for a stably stratified layer can be expressed as $\mu_t = \gamma\kappa w_* L$, with $\gamma \approx 0.2$, $\kappa \approx 0.4$, and L the Obukhov length scale. L can further be related to the upper ocean stability frequency, i.e. the Brunt-Väisälä frequency $N = \left[-\frac{g}{\rho_0} \partial \rho / \partial z\right]^{1/2}$, (neglecting the speed of sound contribution) as $L = w_*^3 / (\kappa \mu_t N^2)$, leading to $\mu_t = \gamma^{1/2} w_*^2 / N$. For more details the paper [RD-8] is recommended, notably regarding (Eq. 13a and 13b). Following this development, the mixing penetration depth can thus be evaluated as

$$\delta = \gamma^{1/4} w_* / \sqrt{fN}. \quad [3]$$

This expression explicitly takes into account the ambient density stratification. Compared to the initial guess, $\delta \sim w_*/f$, it indicates whether wind-induced kinetic energy shall mostly accelerate the surface waters horizontally or contribute to erode the upper ocean stratification. For a Prandtl number $N/f \approx 10$, $f = 10^{-4}$, the turbulent mixing is likely captured in the upper layer. The mixing penetration depth is limited, roughly estimated to be about $\delta \approx 25$ m for a wind speed 10 m/s. For a much less stratified upper layer, $N/f \approx 1$, on the other hand, the corresponding estimated depth is in comparison much larger $\delta \approx 80$ m. Within this typical depth range, the wind/wave/surface current contribution will then spiral (to the right in the Northern hemisphere, positive f) and decay exponentially. The resulting wind-driven current component will then not be expected to be significant at a depth larger than 0.7 times the Ekman depth.

As expressed above within the horizontal momentum equation, such upper ocean spiralling motions must be understood to be relative to and superimposed on a mean motion related to the underlying flow dynamics. Accordingly, despite its wide acceptance, Ekman current spirals can become difficult to observe. Spirals are small signals that can easily be masked by ocean variability and cannot readily be separated from the embedding quasi-geostrophic component.

Moreover, it must be noted that the ratio L/δ is also indicative of the influence of the buoyancy force. For $L/\delta \ll 1$, turbulent friction can strongly decrease, and the top water above a strong thermocline can slide over the underlying ocean with a minimum friction. For instance, strong solar heating warms and stabilizes the surface layer [RD-14]. For large daytime heating and relatively low wind speed (< 4 -5 m/s), the temperature difference

between surface (< 50 cm) and sub-surface (> 3 m) can be 5 times larger than predicted by standard logarithm decay, leading to a temperature difference of about 0.5-1 degree over the first 3 m. This effect can then almost totally suppress the penetration depth of the wind/wave turbulent mixing. The corresponding slipperiness effect should thus be more effective under low wind conditions, also when approaching the equator, where the Coriolis parameter tends to zero, and more efficient in regions of intense diurnal heating. This effect can further result in forming local daytime near-surface anomalous current, possibly reaching about 20 cm/s, independent of wind forcing conditions. Accordingly, the temporal variability of the upper layer stratification, mainly supported by the diurnal cycle under fair weather conditions, can play a major role in the structure of the Ekman layer.

Furthermore, $\vec{\tau}$, the surface tangential forcing interacting with a moving surface, including wave and surface current motions, will also be modified. An air-sea adjustment must be considered to depend upon the atmospheric stability and U_{10} , both also affected by the sea surface temperature (SST), whose spatial distributions are possibly governed by the upper ocean dynamics.

Given an ideal effective wind stress, τ_e , taking into account the effect of surface-velocity dependency (depending upon oceanic and atmospheric stability correction), another adjustment is to further consider the overall modification of the local Coriolis parameter [RD-15] taking into account the modified vorticity, $f + \omega$, with $2\omega = \partial_x v_g - \partial_y u_g$, the local vorticity of the underlying interior flow, e.g. the geostrophic flow (u_g, v_g) . To note, the underlying flow can further result from the superposition of different local motions (geostrophy, tidal, dampened inertial contributions). Accordingly, considering a well-mixed upper ocean, i.e. winter conditions, an effective surface forcing will thus act below the wind/wave layer (scaling with the wind sea significant wave height, H_{sw} , or 0.5 m for $U_{10} < 4 - 5$ m/s), to produce, from this depth, $z < H_{sw}$, upper ocean surface currents of the form

$$\begin{aligned} U_{upper}(z) &= u_g + \frac{\sqrt{2}}{\rho_0(f + \omega)\delta} e^{z/\delta} \left[\tau_e^x \cos\left(\frac{z}{\delta} - \frac{\pi}{4}\right) - \tau_e^y \sin\left(\frac{z}{\delta} - \frac{\pi}{4}\right) \right] \\ V_{upper}(z) &= v_g + \frac{\sqrt{2}}{\rho_0(f + \omega)\delta} e^{z/\delta} \left[\tau_e^x \sin\left(\frac{z}{\delta} - \frac{\pi}{4}\right) + \tau_e^y \cos\left(\frac{z}{\delta} - \frac{\pi}{4}\right) \right] \end{aligned} \quad [4]$$

As derived, this simplified decomposition solely corresponds to steady solutions of the horizontal momentum equation within a well mixed homogeneous density layer, more likely corresponding to winter conditions, i.e. the Obukhov length scale L and H_{ML} are large, with steady underlying flow conditions u_g, v_g, ω , under a stationary temporal forcing, τ_e over a few inertial periods.

Corresponding to more marked upper ocean stratification, e.g. summer conditions, the mixing penetration depth is limited. The upper current speed will still decrease with depth following an e-folding spiral. Yet, the current will likely be intensified near the surface to then decrease with depth more rapidly than the current vector shall rotate. Accordingly, the spirals must be compressed in the downwind direction. The boundary condition, $(u, v) \rightarrow (u_g, v_g)$, now applies to an expected shallower depth compared to well-mixed conditions, limited to the mixing penetration depth. For such a case, kinetic energy goes into accelerating the surface drift. For steady conditions, the upper ocean surface currents can then be heuristically formulated as

$$U_{upper}(z) = u_g + \frac{\sqrt{2}}{\rho_0(f + \omega)\delta^*} e^{z/\delta^*} \left[\tau_e^{*x} \cos\left(\frac{z}{\delta^*} - \frac{\pi}{4}\right) - \tau_e^{*y} \sin\left(\frac{z}{\delta^*} - \frac{\pi}{4}\right) \right]$$

$$V_{upper}(z) = v_g + \frac{\sqrt{2}}{\rho_0(f+\omega)\delta^*} e^{z/\delta^*} \left[\tau_e^{*x} \sin\left(\frac{z}{\delta^*} - \frac{\pi}{4}\right) + \tau_e^{*y} \cos\left(\frac{z}{\delta^*} - \frac{\pi}{4}\right) \right] \quad [5]$$

By considering $\delta^* < \delta$, and $\tau^* > \tau$, the obtained spiral will be compressed in the downwind direction. Accordingly, the tangential stress is seemingly intensified. This can somehow correspond to a marked singularity of the turbulent eddy viscosity parameter, near the surface. In such a case, the surface boundary conditions $(A_{z=0} u_z^e)_{z=0} = \tau/\rho_w$ can lead to particular solutions. Yet, a vertical average of the linear momentum equations over the mixed-layer (ML) depth H_{ML} (assumed constant over the whole domain), must still recover the integral volume transport as

$$\int_0^{H_{ML}} \frac{u_g}{H_{ML}} dz - \frac{\tau}{\rho_0(f+\omega)H_{ML}} \quad [6]$$

To note, the first integral term can further take into account the possibility that vertical mixing can indirectly affect horizontal motions within the mixed-layer depth. From scale decomposition, the small components contributing to the geostrophic velocities will be more affected than the large ones, as smaller scales, likely corresponding to very sharp density gradients, have smaller vertical extension.

Note, for less homogenous conditions, the model framework can also be used to illustrate some of the main mechanisms leading to the generation of ageostrophic secondary circulation (ASC). According to the proposed simplified decomposition, spatial variations of the effective stress can be considered first. This leads to flow divergence and consequently generation of vertical velocities $w = \frac{1}{\rho_0(f+\omega)} (\partial_x \tau_0^y - \partial_y \tau_0^x)$, the so-called Ekman pumping mechanism.

Another mechanism is related to the advective interaction of the Ekman flow with the underlying flow to trigger ASC currents related to the underlying spatial variations of the flow (e.g. [RD-16]), as

$$U_{ASC} = -\frac{1}{f(f+\omega)\delta} (\tau_e^y \partial_x v - \tau_e^x \partial_y v) \text{ and } V_{ASC} = \frac{1}{f(f+\omega)\delta} (\tau_e^y \partial_x u - \tau_e^x \partial_y u). \quad [7]$$

Note that the effective stress, τ_e , shall further adjust to these upper ocean circulation changes, further prompting some effective Ekman pumping contribution. Furthermore, these spatial variations of the underlying flow can often be associated with SST (density) fronts. Again, τ_e will certainly adjust to the SST fronts with correlated spatial variations. Moreover, frictional effect in the Ekman layer will further lead to the ASC components (e.g. [RD-17]; [RD-8]) expressed as

$$U_{ASC} = -\frac{\mu_t g}{\rho_0 f^2} (\partial_{zx}^2 \rho) \text{ and } V_{ASC} = -\frac{\mu_t g}{\rho_0 f^2} (\partial_{zy}^2 \rho), \quad [8]$$

leading to vertical velocities proportional to the Laplacian of the density field (SST and SSS).

6. Summary and Outlook

Based on the discussion and analysis given above, the ocean surface current (OSC) estimates will essentially rely on using the following parameters:

- U_{10} , atmospheric stability, sea state information (Stokes drift estimates, H_{sw} , coupled

- drag coefficient);
- SST, SSS, top layer stability information (diurnal heating, intense precipitation), mixed layer information (temperature and salinity stratifications, depth);
- Local (u, v) underlying flow information (tidal current, absolute mean dynamic flow), and connection to the strength of SST and SSS fronts;
- τ_e an effective upper ocean forcing below the top layer, i.e. H_{sw} .

Considering a direct identification between Eq. 5 and the measurable residual upper surface current, a practical solution is finally expressed as

$$\vec{U}_{upper}(z) = \vec{U}_g^{alt} + \vec{U}_{residual}(z) = \vec{U}_g^{alt} + \beta(z)\vec{U}_{10}e^{i\theta(z)} \quad [9]$$

where $\beta(z)$ and $\theta(z)$ are to be empirically determined locally and seasonally, using filtered wind estimates, \vec{U}_{10} . For $z = 0$ large-scale altimeter-derived geostrophic velocities are subtracted from the Argo surface velocities, while for $z = 15 \text{ m}$, these geostrophic velocities are subtracted from the 15 m drogued SVP buoy velocities.

Primarily considering this simplified decomposition given by eq. 9, the critical determination of the underlying flow information, e.g. \vec{U}_g^{alt} , mostly builds on available medium-resolution satellite observations (altimetry, SST and more recently SSS radiometry). In addition it fully benefits from a more accurate knowledge of the ocean's mean dynamic topography (MDT), building on the consistent joint-analysis of gravimetry, altimetry and in-situ observations (e.g. Rio et al., 2014). Thanks to the improved resulting MDT the global OSC products can be derived at approximately 30 km (tentatively 10 km) spatial resolution. Given this length scale, a characteristic temporal scale (i.e. sketch Figure 13 and Figure 14) in consistence with this wavelength is about 3 days. OSC products can further include more rapidly time-varying components, such as tidal currents, wind-wave-related information, and may possible also include diurnal heating estimates, to provide products at different temporal resolution, typically 3-hourly.

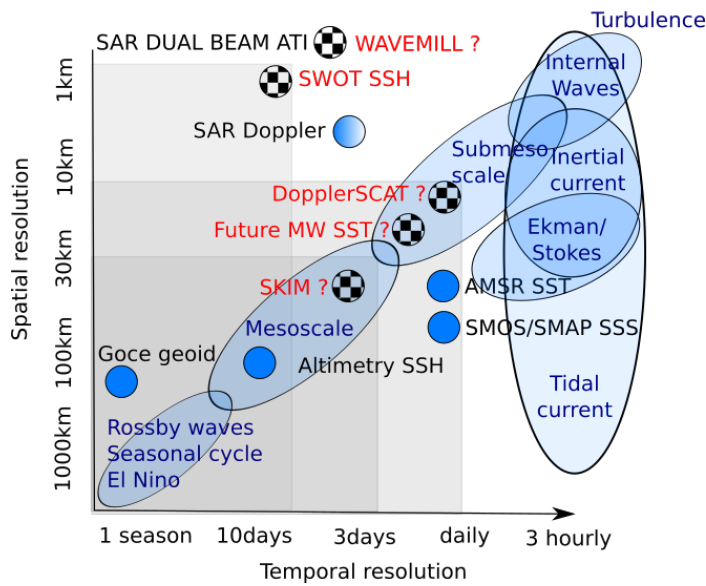


Figure 14: Spatial and temporal scales of key upper ocean surface current features overlaid and mapped into a selection of existing and future approved and planned satellite duty cycles and sampling coverage typical representative for mid-latitudes.

So in view of the main findings and achievements from the GlobCurrent project and the characteristics of spatial and temporal scales projected onto the typical satellite sampling coverage and repeat cycles (see Figure 14) we have reached a more consistent understanding for how well the total surface current are observed from space. This has been complemented and further strengthened by:

- An improved and more accurate mean dynamic topography (MDT) for retrievals of the GlobCurrent global and regional (Mediterranean Sea) products. Further efforts are planned to especially derive higher-resolution MDT estimates.
- A range of tools that has been developed and applied in the GlobCurrent project (now available) showing distinct capabilities to advance the analyses and interpretation of the remote sensing data (e.g. Lagrangian approach, ray tracing, MCC, eddy tracking, SST-SSH correlation, singularity exponent, etc.).
- Unexpected Sentinel-2 findings and capabilities to retrieve surface wave phase velocity including the underlying surface current. This is really inviting the consideration to fly Sentinel-2C in an optimum tandem with Sentinel-3C for quantitative exploration and validation of surface current retrievals.
- Analyses and interpretation of merged SST with SSH fields and some SSS fields started late, but with preliminary promising findings. This will now be further investigated and explored for operational production within a new CCN-3 study to be kicked-off in beginning 2018. This study may also benefit future investigation of joint passive microwave SST and SSS (C-band and L-band) mission at higher spatial resolution.

However, the GlobCurrent project also encountered some unforeseen challenges and deficiencies. In particular:

- We had anticipated the use of Sentinel-1 Range Doppler. Disappointingly the Doppler signal has not become available, hence no retrieval of high resolution mean surface current, in particular in the equatorial currents, western boundary currents, shelf currents and currents in the marginal ice zones.
- We had anticipated more systematic use of SAR altimetry to allow high-resolution SSH observations across strong western boundary and coastal currents as well as in vicinity of the ice edge in the marginal ice zones.
- The late availability of Sentinel-3 data unfortunately inhibited the opportunity to fully explore the sensor synergy between Sentinel-1, -2 and -3, in particular the combined retrievals of along track SAR altimetry with maps of SST, ocean colour and surface roughness. Such an investigation is highly recommended for a future study. Equally so is exploration of Sentinel-3 tandem for MCC type applications.

The User Consultation Meetings strongly favoured the production and delivery of near real time GlobCurrent products. This will be secured through a GlobCurrent CCN-3 study that will be launched in January 2018 for a 9 months duration. Moreover, the observation of surface current from space is also encountering a promising future, both in regards to upcoming approved missions as well as initiation of Phase A studies of potential new future mission as indicated below:

- The approved Radarsat constellation will strengthen the opportunity to enrich the high-resolution snapshot imaging for upper ocean process studies.
- The approved SWOT mission with tentative launch in 2021 aims to improve the spatial resolution of the mesoscale surface geostrophic currents.
- The Earth Explorer 9 (EE9) candidate mission, SKIM, which is a dedicated mission for total surface current retrievals, including both geostrophic and ageostrophic components

(distinctly different from SWOT) have recently been approved for Phase A. Based on the GlobCurrent project findings and achievements a careful investigation on how to maximize this mission through a constellation approach is highly recommended to further enhance and strengthen the analyses and interpretation framework for upper ocean dynamics. This will also be highly beneficial for validation of future coupled high-resolution ocean-atmosphere models.

In closing it should also be emphasized that the GCOS-200 (*THE GLOBAL OBSERVING SYSTEM FOR CLIMATE: IMPLEMENTATION NEEDS*) document has identified the surface current is an Essential Climate Variables (ECV). On basin scales, surface currents and their variations are a major player in climate to weather fluctuations. Parameterized wind stress and heat flux depend upon the speed of the near-surface wind relative to the moving ocean surface, which can be significantly affected at large scales by surface currents such as the western boundary currents and Antarctic Circumpolar Current, and at smaller scales by mesoscale variability. Moreover, surface current convergences/divergences, spiraling eddies, and filaments all contribute to vertical motions and mass exchange. Surface currents also impact the steepness of surface waves, and are important for generating accurate marine sea state forecasts. Because of their significance in advecting passive particles, knowledge of surface currents is also important for applications associated with oil spill and marine debris response, search and rescue operations, and ship routing. Currents, particularly tidal currents, can also modify storm surge impacts and sea level changes.

Annex 1.1: GlobCurrent Observational Framework

Direct and (mostly) indirect estimates of OSC, and higher level derived quantities such as frontal boundaries (see for instance Figure A1.2 and <https://odl.bzh/92dPfsMh>), can be derived using a variety of satellite sensors including altimeters (both LRM and SARM), gravimetry instruments, SAR imagers, scatterometers, optical (VIS and TIR) and passive microwave imaging instruments. Sparse but increasing, in-situ surface current measurements from drifting and moored buoys, coastal HF-radar installations, Argo floats, gliders and ship observations also complement these multi-mission multi-instrument observations. This is illustrated in Figure A1.1 giving an overview of the links between observation platforms, sensor types, observed ocean variables and derived quantities associated with ocean surface current phenomena. As noticed the Sentinel-3 radar altimeter, infrared radiometer and imaging spectrometer (including sun glint) observe 6 geophysical variables, notably: sea surface height (SSH), significant wave height, near surface wind speed, sea surface temperature (SST), ocean colour and small scale roughness anomalies. These variables and their spatial and temporal changes contain direct or indirect manifestations and signals related to the surface current conditions, notably: surface geostrophic current, Stokes drift, surface Ekman current; inertial motion; surface current boundaries; surface tracer velocity; and surface current vorticity (as also specified in Figure 13 and Figure 14).

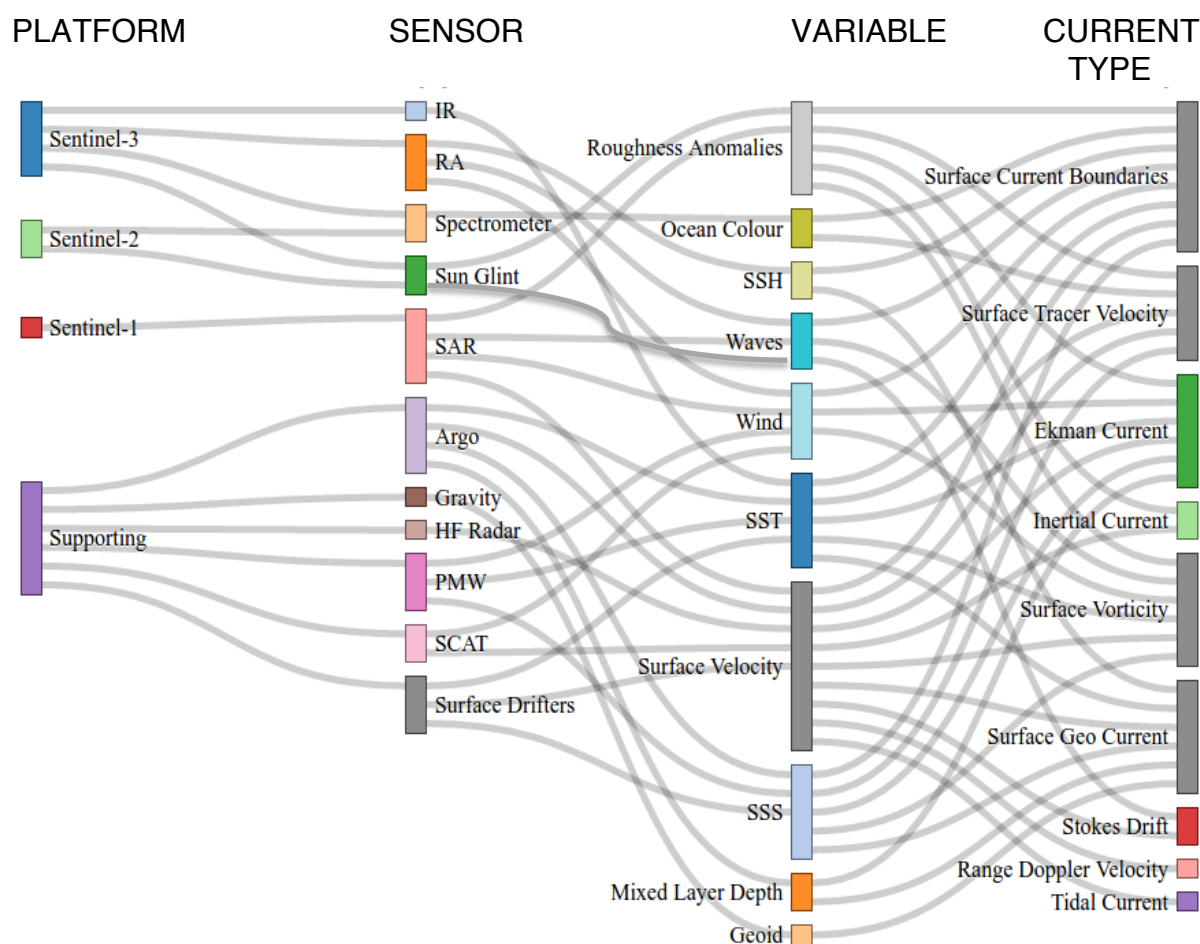


Figure A1.1. Illustration of combined Sentinel-3, Sentinel-2 and Sentinel-1 provision of data and information products in support to the global, regional and local surface current estimations. Additional provision of complementary data and information other supporting missions (including SMOS and GOCE) and in-situ data (Argo, drifters) further demonstrates the importance and strength of the systematic use of sensor synergy.

Systematic use of satellite sensor synergy combined with in-situ data, all with their specific strength and set of limitations (e.g. resolution, spatial-temporal coverage, accuracy, depth integration, cloud dependency, empirical-based retrieval methods, etc.) will therefore strengthen our ability to obtain high quality and consistent information on surface current phenomena and their relationship to the upper ocean (~100 m) dynamics and processes. This is highlighted in Table A.1.1.

Existing Satellite measured quantity (sensor)	Retrieval Model	Surface current component	Depth and spatio-temporal resolution	Accuracy
Sea level anomaly from altimeters (conventional and high resolution SAR)	Geostrophic assumption	Geostrophic current anomaly	Subsurface Optimal interpolated gridded field, every 10 days at 30 km resolution.	TBD
GOCE	Geoid	Mean dynamic topography	Mean geostrophic current at spatial scale of 100-200 km	1-2 cm
Altimeter + GOCE	Sea surface height and geoid	Absolute dynamic topography	Absolute surface geostrophic current at spatial scale of 30 km. May even be finer (~10 km) with access to SARM altimetry data	Seasonal and regional accuracy dependency.
Microwave SST, SSS	Surface Quasi Geostrophy, statistical analysis, Optical flow methodology	Geostrophic current anomaly Stability (related to air-sea temperature difference) information	Subsurface 12 hourly at 25 to 50 km resolution.	Seasonal and regional accuracy dependency.
Range Doppler velocity (SAR) from Sentinel-1	CDOP sea state component of Doppler shift	Radial component of total current minus wind drift (included in CMOD)	Depth = significant wave height Wave mode products: monthly at 2°, Wide swath products: seasonal at 10km.	Wide swath (30cm/s snapshot, 5cm/s for the mean). Wave mode (10cm/s for the mean)
10 m wind vectors (Scatterometers, merged products)	Surface stress estimates Ekman model	Surface wind drift Ekman transport	within the Ekman layer, 12 hourly, 12.5 km	Drag coefficients (sea state, stability) Vertical profile definition in presence of sea state and underlying currents. TBD
Swell wavelength and direction (SAR) from Sentinel-1 and Sentinel-2	Wave current interaction (wave refraction by varying current)	Vorticity of total current	Depth = significant wave height weekly at 25km.	SAR swell imaging properties, and relative ratio between vorticity and swell group velocity TBD
Infrared SST, ocean color, Sun	Optical flow methodology	Total front (orientation,	Polar orbiting: daily at 10km (TBC) resolution	Depending upon the strength of the

glitter and SAR roughness (from Sentinel-1, Sentinel-2, Sentinel-3)	Frontal detection	strength, related to local deformation field) locations and occurrences	provided cloud free and feature presence. Geostationary : 3 hourly at 25km (TBC) resolution provided cloud free and feature presence. Frontal climatologies (25km to 5 km, day, week, month)	gradients to delineate and associate surface feature manifestation.
Drifter velocity (IRIDIUM, ARGOS)	None (direct)	Total Lagrangian (including Stokes drift) at surface, total minus wind drift and Stokes drift at 15m	0 to 15m depending on drogue depth monthly at 0.5° resolution (from NOAA analysis)	<10cm/s Temporal filtering TBD
Argo floats	None (direct)	Temperature, salinity, MLD Lagrangian motion	0 to 1000 m Individual profiles Monthly at 2° resolution 0 m	QC

Table A1.1: *Observational platforms and the ocean surface current component information that can be observed from them.*

Annex 1.2: GlobCurrent data-driven SST-SSH Framework

The wide spacing between the altimeter satellite ground tracks is known to limit the cross-track resolution to several hundred km. Hence, satellite altimetry data cannot resolve the smaller scales (20-100km) of the embedded highly dynamical flows that are often revealed on high-resolution optical, infrared and radar images. This is further evidenced and illustrated by the so-called “dog head” feature (Figure A1.4).

In cases when the upper ocean is well mixed, as for instance during winter, the interior geostrophic motions can be constrained by the SST and SSH anomalies. This is clearly depicted in Figure A1.2 where gradients in SST and SSH are averaged and compared for the month of February 2008 at wavelengths from 100-300 km. As readily obtained, the emerging and rich mesoscale circulation from SSH measurements, apparently stirs the large-scale SST fields. Several studies rationalize and demonstrate that fields of SST (a proxy of the upper layer density) can indeed become an active tracer coupled to the dynamics, leading to strong correlations with SSH fields. A qualitative inspection of the filtered SSH and SST global fields (Figure A1.3) does not contradict such an assumption. A basic idea is therefore to look for the best local relationship between the SST anomaly and the potential vorticity anomaly to help recognize the link between SST and SSH anomalies. In so doing the empirically-derived vertical profile function calculated from the large scale potential vorticity and surface temperature gradients can be adjusted to recover the interior potential vorticity anomaly $PV'(x, y, z) = \nabla^2 \psi' + \partial_z \left(\frac{f^2}{N^2} \partial_z \psi' \right)$ and $\rho'(x, y) = -\frac{f\rho_0}{g} \partial_z \psi'(0)$, with ρ_0 as the reference density, and invoking a lower boundary conditions of the form $\partial_z \psi'(H) = 0$.

An empirically-derived relationship is then written as $PV'(x, y, z) = \alpha(z)\rho'(x, y)$, with $\alpha(z)$ related to large-scale meridional gradients that can first be evaluated from large-scale in situ measurements, e.g. $\alpha(z) \approx \partial_y \overline{PV(z)} / \partial_y \bar{\rho}$ or $\alpha(z) \approx \langle \partial_y PV \cdot \partial_y \rho \rangle / \langle \partial_y \rho^2 \rangle$, to capture the

correlation between potential vorticity and density in the upper ocean (300-500 m). Considering that $\alpha(z)$ projects onto the first baroclinic mode, and also N taking as constant, a solution for the stream function can readily be obtained for very large H , to write in the Fourier domain

$$\hat{\psi}(z) = -\frac{\alpha(z)\hat{p}}{K_1^2 + K^2} + \frac{g\hat{p}}{NK} e^{NKz/f} \quad [\text{A.1}]$$

where K is the isotropic horizontal wavenumber, and K_1 the first baroclinic wavenumber. Accordingly, the stream function is recognized as a smooth function of the upper ocean density, as the weight of the smaller scales (larger K) are attenuated as $1/K$, corresponding to a spatial filter in $1/\sqrt{x^2 + y^2}$. To note, the vertical mixing within the mixed-layer depth, D , can affect the near-surface horizontal motions. Its impact is expected to be stronger for small scales than for larger ones, as smaller scales (large K) have smaller vertical extension ($f/NK \leq D$) to be more efficiently damped. Vertical motions act to further smooth the vertical profile of the horizontal motions. In response, a vertical circulation develops to possibly restore the thermal wind balance, with vertical velocities proportional to the Laplacian of the density field (Eq. 8).

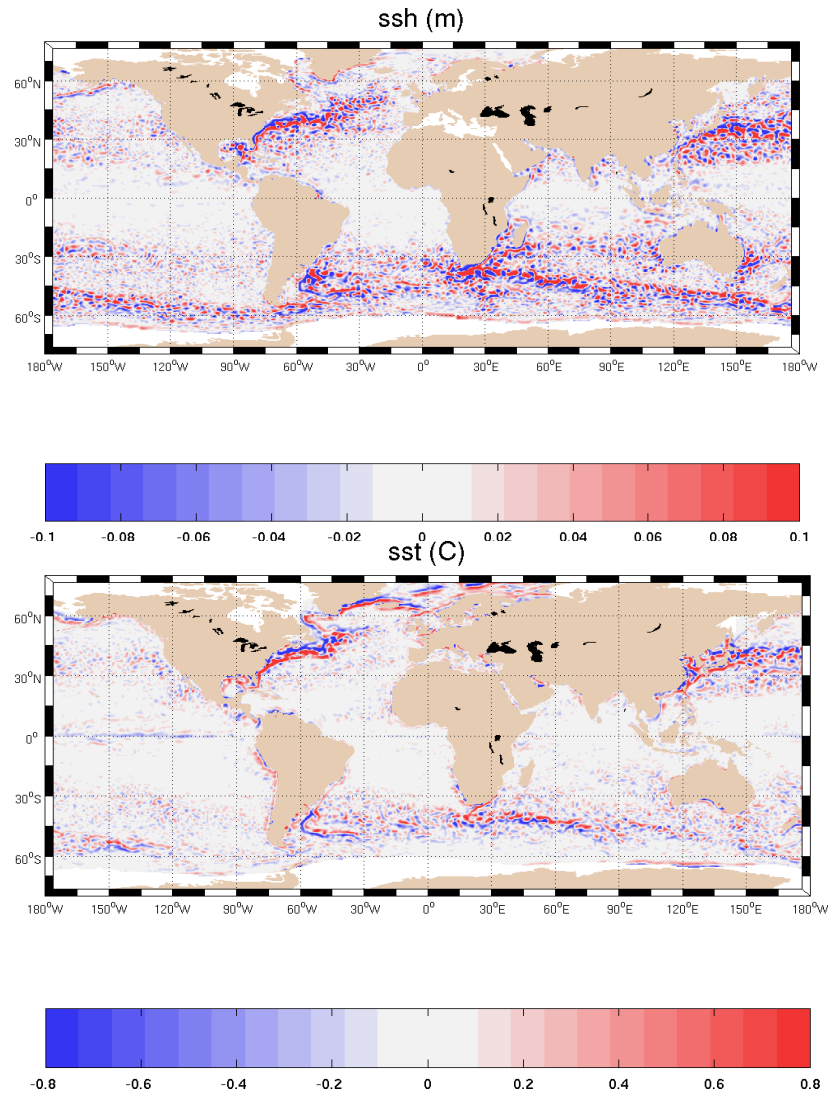


Figure A1.2: Mean SSH gradients (upper) and SST gradients (lower) for February 2008.

This approach strongly advocates for observation-driven studies to explore and characterize the local relationships between SST, SSH, possibly SSS and the derived surface currents from satellite-based routine observations (e.g. [RD-21, RD-22]). However, as illustrated in Figure A1.3, a simple linear transfer function cannot be expected to solely govern the whole mesoscale dynamics in a particular ocean region. As revealed, an overall spatial correlation exists, but for instance, relationships between SST gradients and altimetry-derived surface currents may spatially differ. In the warmer SST frontal zone, the SST gradients correspond to the large surface currents (top of the image). In the colder frontal area, on the other hand, the larger scale SST gradients do not reflect the larger surface currents (bottom of the image). Moreover, the clearly detected eddy (top left of the image) is associated with weak SST gradients.

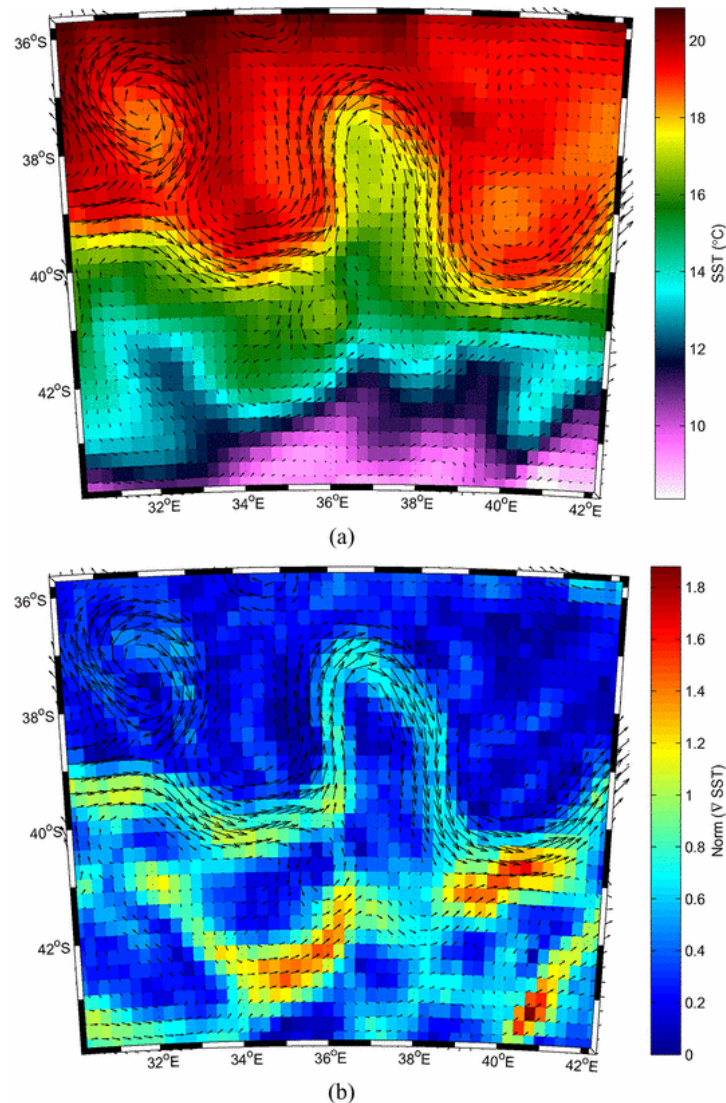


Figure A1.3: Surface currents derived from altimeter SSHs and (a) microwave SSTs and (b) the associated temperature gradient norms within the Agulhas return current on January 1, 2004.

In the GlobCurrent project the daily fields of SST and surface geostrophic current are regularly combined and blended (at regional scale) with snapshot observations such as ocean colour, sunglint and Sentinel-1 SAR roughness anomaly as well as other Level 2 to 4 products. An example of this is depicted in Figure A1.4 whereby a Sentinel-1 SAR surface roughness image is overlying the combined surface geostrophic current and SST field and along-track sea surface height from radar altimeters centered to 23 March 2015.

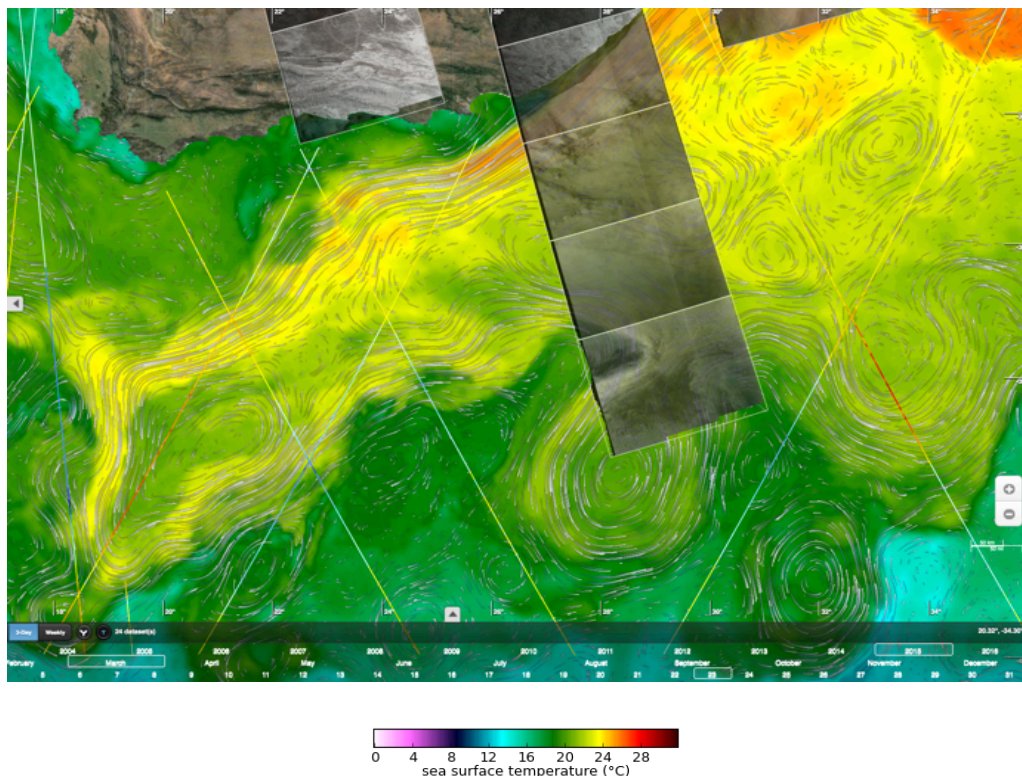


Figure A1.4: Synoptic snapshot of the so-called “dog head” feature showing the combined 2-D SST map (colour), surface geostrophic current (stippled streamlines), and surface roughness from the Sentinel-1 SAR image obtained on 23 March 2015. The sea surface height track data from radar altimetry are also overlaid. The color bar gives the SST in degree Celsius.

Due to the lack of temporal resolution in altimetry as exemplified in Figure A1.4 the surface geostrophic velocities derived from altimeters are not always consistent with the SST observations, especially in the presence of sharp frontal boundaries. A strategy to correct for such sampling discrepancy has been implemented (e.g. GlobCurrent D-160: ATBD-3) and will be further investigated and tested in and upcoming CCN-3 study.

Annex 1.3: GlobCurrent Lagrangian Approach

The Lagrangian lateral advection can be used to transfer large to medium scale tracer fields to frontal positioning and cross-frontal tracer gradients at a finer spatial resolution as shown in Figure 4. This methodology can be jointly applied to any surface tracer field (ocean colour, sea surface salinity, sea surface temperature, etc) to introduce finer-scale structures at the final time of advection [RD-24]. Figure A1.5 provides an example for how one may compare medium-resolution surface temperature fields derived from passive microwave observation (50 km resolution) with a cloud-free high-resolution IR field from optical imagery (MODIS at 2-5 km resolution). The separation time between observations is 12 days. As demonstrated, small-scale features are often well captured and can thus allow the reconstructed fields to be compared with cloud-free observations.

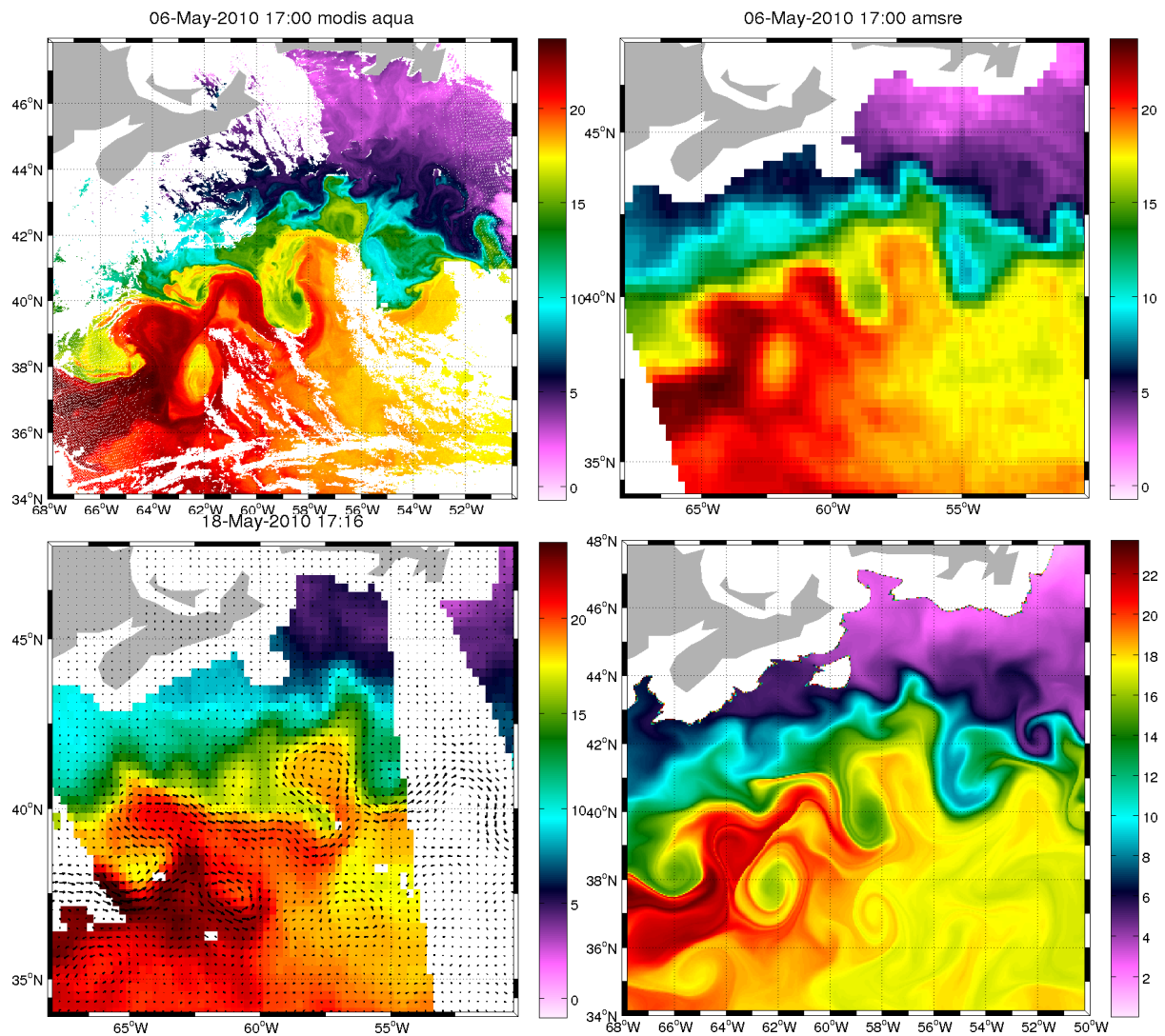


Figure A1.5: Illustration of Lagrangian advection in the Gulf Stream region to dynamically interpolate medium-scale surface temperature (passive microwave AMSR-E surface temperature field, bottom left) onto a high-resolution product (bottom right). Backward particle trajectories computed using altimetry-derived velocities (AVISO, weekly 1/3°) with 3 hours time steps to compare with previous observations (12 days backward), i.e. high-resolution MODIS sea surface temperature (top, left) and medium-resolution AMSR-E sea surface temperature (top, right)

As further noticed in Figure A1.5 the advected tracer field will exhibit thin and elongated filamentary patterns to strongly diverge from real observations after some days. As such, the parameters to control the advection (total number of days, time steps and spatial resolution, diffusion) will strongly depend on the applicability of the 2D advection in the evolution of the tracer field for a particular dynamical region. The possibility to apply this method to different tracer fields (e.g. sea surface temperature, sea surface salinity, ocean colour) will help to further assess the links between the 2D surface signatures and the underlying distribution of the upper ocean dynamics. Using large swath satellite data, the observations can reveal a wide range of sizes and a variety of shapes, with a large occurrence of frontal systems (Figure A1.6). Consequently, this textural richness leads to continuous spectral estimates that span a very wide range of scales. Variances of these different scales are further often found to follow constant power-law distributions. However, the spectral forms may only be a very weak constraints concerning the structure of the underlying flows, as coherent structures essentially sign in the phase information of the satellite snapshots as illustrated in Figure A1.6.

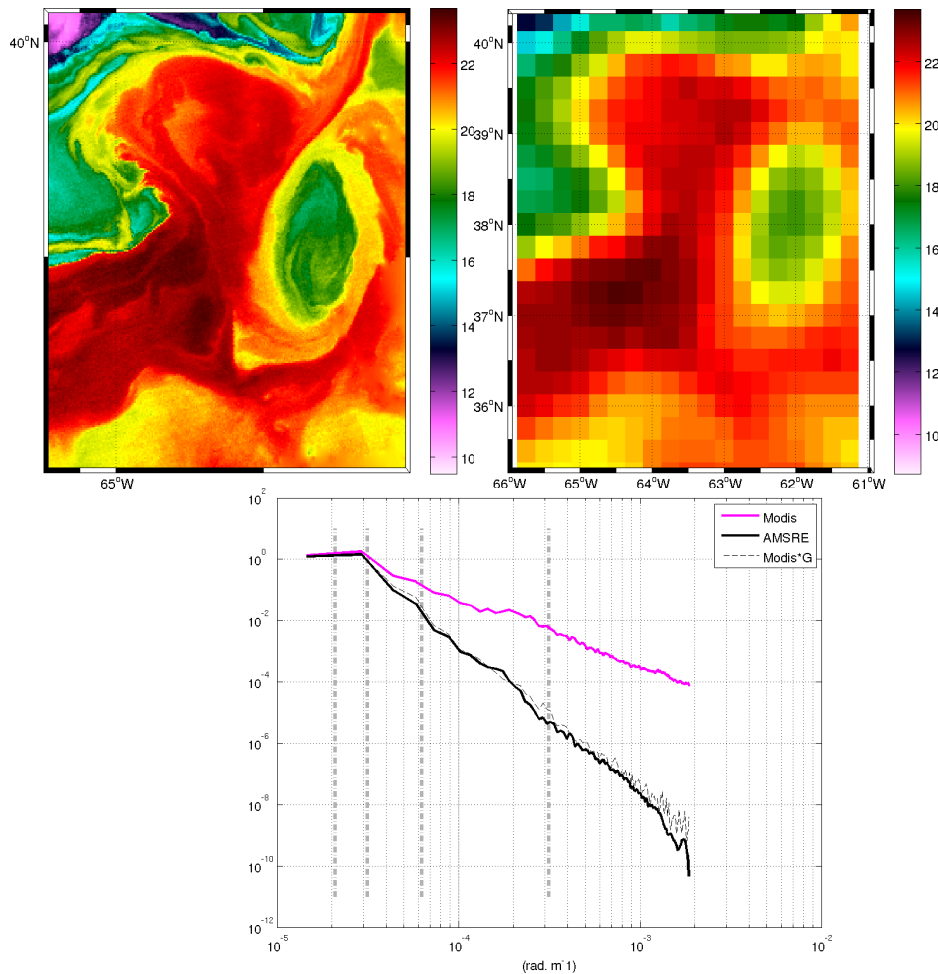


Figure A1.6: Contemporaneous sea surface temperature fields from MODIS (upper left) at 2 km resolution, and AMSR-E (upper right) at 25 km sampling resolution. Spectral analysis (lower) illustrates the impact of instrumental smoothing effect on AMSR-E (passive microwave) observations to strongly increase the spectral roll-off, starting at 100 km scale. Comparisons are given with filtered and non-filtered MODIS observations.

In this figure the passive microwave observations correspond to a smoothed version of the high-resolution field, to possibly become closer to a stream function. Indeed, as already mentioned and illustrated Figure A1.2, the sea surface temperature and the sea surface height are likely highly correlated to trace the ocean interior potential vorticity. Correspondingly, a direct use of filtered temperature and salinity observations, from passive microwave observations (SMOS, AMSR-2), can provide means to derive first guess stream functions. Importantly, these observations benefit from the ability to operate through clouds to provide dense temporal samplings, i.e. daily to 3-day global coverage.

Subsequently, to gain more insights, the expected higher temporal resolution shall be compared to Lagrangian-derived tracer fields (Figure A1.5, bottom right) to more directly constrain and strengthen the analysis of the geometry and complexity of delineated structures, for instance as derived from the analysis of level sets and fronts. As proposed, this can further help the characterization and interpretation of the underlying flow properties. Indeed, line stretching and bending are main characteristics generally driven by both local small scales and non-local larger scales of the velocity fields. Surface contour statistics and frontal characteristics can thus further help to better understand the internal organization of the flow, as earlier suggested by [RD-25] and the use of the surface quasi-geostrophy dynamics.

Annex 1.4: Obuko-Weiss Approach

Under the simplified assumption to consider tracer conservation along a Lagrangian trajectory, efficiency of these interactions can be attributed to the phase shift between the tracer field and the streamfunction, e.g. SST (and/or SSS) and SSH fields. Indeed, the time evolution of a tracer gradient, q , advected along a Lagrangian trajectory verifies the equation $Dq/dt = -[u]^*q$, where $[u]^*$ is the transpose of the velocity gradient tensor, that can be decomposed in 3 parts: vorticity $\omega = \partial_x v - \partial_y u$, normal strain $S_1 = \partial_x u - \partial_y v$, and shear strain $S_2 = \partial_x v + \partial_y u$. The eigenvalues of the velocity gradient tensor are $\pm\sqrt{\lambda}$ with $\lambda = 1/4 (S_1^2 + S_2^2 - \omega^2)$. The quantity λ has been derived by Okubo (1971) and Weiss (1991), and can provide a very efficient criterion to partition the fluid into regions with different dynamical properties from the point of view of tracer gradient evolution. Indeed, along the Lagrangian trajectories, the gradient cannot intensify in vortex-dominated regions, i.e. $\lambda < 0$ leading to purely imaginary eigenvalues. Contrary, gradients are expected to intensify in strain-dominated frontal regions, i.e. $\lambda > 0$, leading to exponential growth with time in such regions. Accordingly, these regions could correspond to convergence or divergence of the stream function field. The eigenvalues having opposite sign, a preferred direction will thus be enhanced, with evolving patterns as elongated filaments. Considering a vector notation to express the relative orientation of the tracer gradient as $q = q(\cos \theta, \sin \theta)$ and $(S_1, S_2) = S(\cos 2\phi, \sin 2\phi)$, the full orientation dynamics then reduces to $D\zeta/Dt = \omega + 2 D\phi/Dt - S \cos \zeta$, with $\zeta = 2(\theta + \phi)$. The gradient magnitude evolution then writes $\frac{2}{|q|} D|q|/Dt = -S \sin \zeta$.

To note, the parameter $r = (\omega + 2 D\phi/Dt)/S$ generalizes the Okubo-Weiss criterion as it also measures the competitive effects between rotation effects, i.e. vorticity ω and rotation of the strain axis $2 D\phi/Dt$, and straining effects. Under the assumption that r is slowly varying in time, large gradients are expected to align with the direction $\zeta_o = -\cos^{-1} r$, with $r^2 < 1$, e.g. strain-dominated frontal regions.

Very interestingly, it must be noted that for a surface QG approximation, the level sets of the surface density (or SST to simplify) are analogous to vortex lines for a 3D Euler incompressible turbulence description [RD-26]. In particular, if $\kappa = (\xi \cdot \nabla \xi) \cdot \xi^\perp$, with $\xi = q/|q|$, denotes the curvature of a level set, one identity is $D(\kappa|q|)/Dt = (q \cdot \nabla)[((\nabla u) \cdot \xi) \cdot \xi^\perp]$. This identity implies that the integral of $\kappa|q|$ on a closed level set is conserved, to give the rotation number of that level set. Under the assumption that the curvature does not oscillate rapidly and strongly, the curvature must adjust (i.e. reduce) to a gradient change (i.e. straightening). Strong gradients are thus expected to strongly align along given directions. In weaker gradient regions, level sets will likely meander. Winding angle statistics, applied to high resolution SST, strongly confirm this type of identity.

We could also include the combined use of the SSH and the SST for frontal sharpening. This would be illustrating the limitation of time-space interpolation when using the altimetry map. It also illustrates the value of snapshot (in this case passive microwaves SST) observations for bypassing the limitations when using the altimetry maps.

Annex 1.5: Wave-Current Refraction

Wave-current refraction has long been known as key indicator of strong surface current vorticity and can be both observed in high-resolution SAR and sunglitter images, and modeled using wave action conservation applied to the incident swell wave period and direction together with surface current vector field such as GlobCurrent global gridded products (Figure A1.7). The comparison of observed and modeled wave transformation by surface current can thus be used to assess the performance of GlobCurrent products gradients and more specifically the derived vorticity field. For this strong current regime the derived wave current refraction is quantitatively agreeing with the SAR observations (Figure A1.7 and A1.8). As noticed, the expected wave refraction is a bit weaker than the SAR detected wave-rays as the vorticity is certainly less pronounced, indicating a slight underestimation of the surface current gradients at the edges of the Agulhas Current.

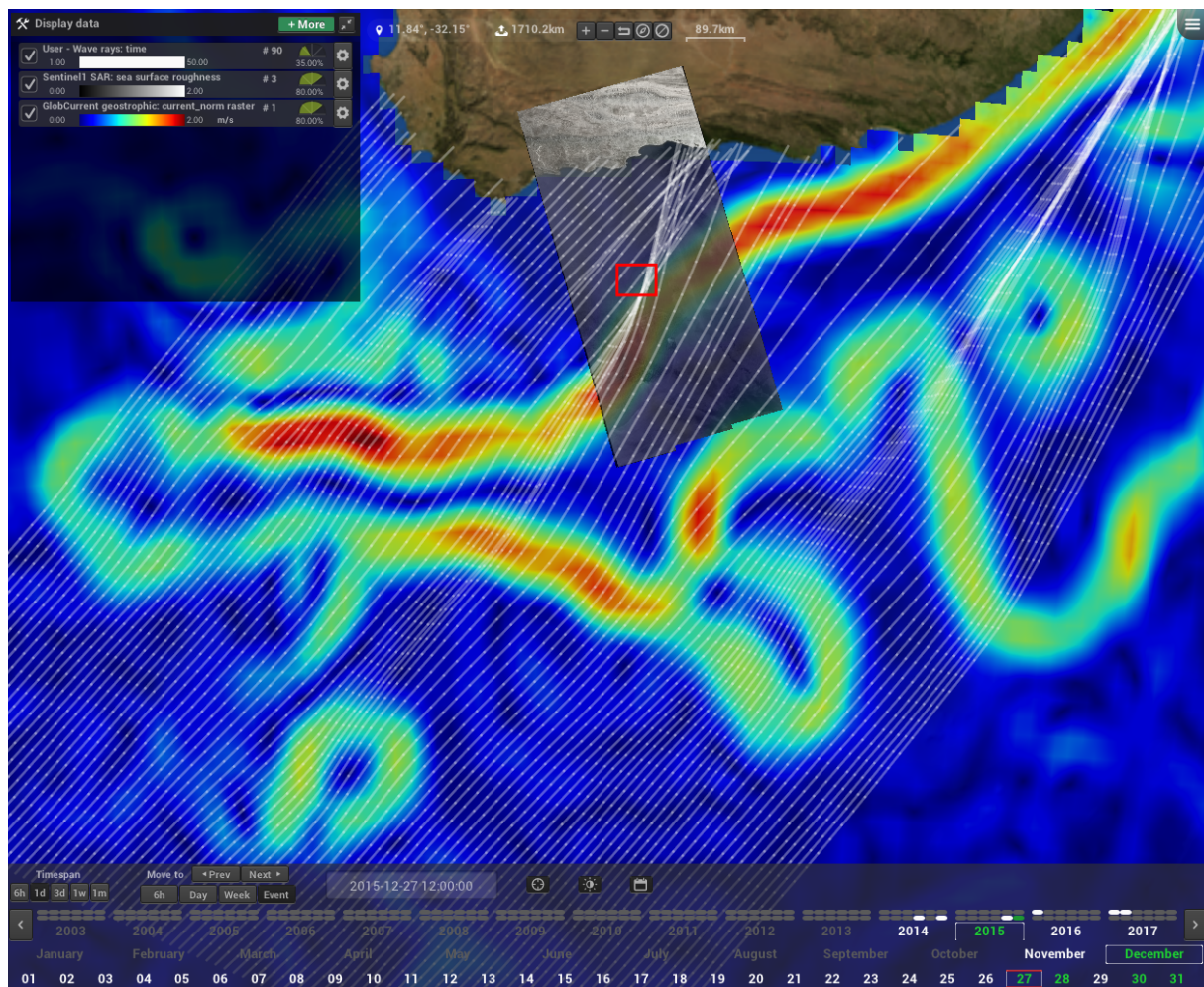


Figure A1.7: Contemporaneous GlobCurrent geostrophic surface current velocity and Sentinel-1 SAR image on Dec 27, 2015. White trajectories are simulated wave propagation path distorted by surface current vorticity. Red rectangle highlights the area of resulting crossing swell detailed on Figure A1.8.

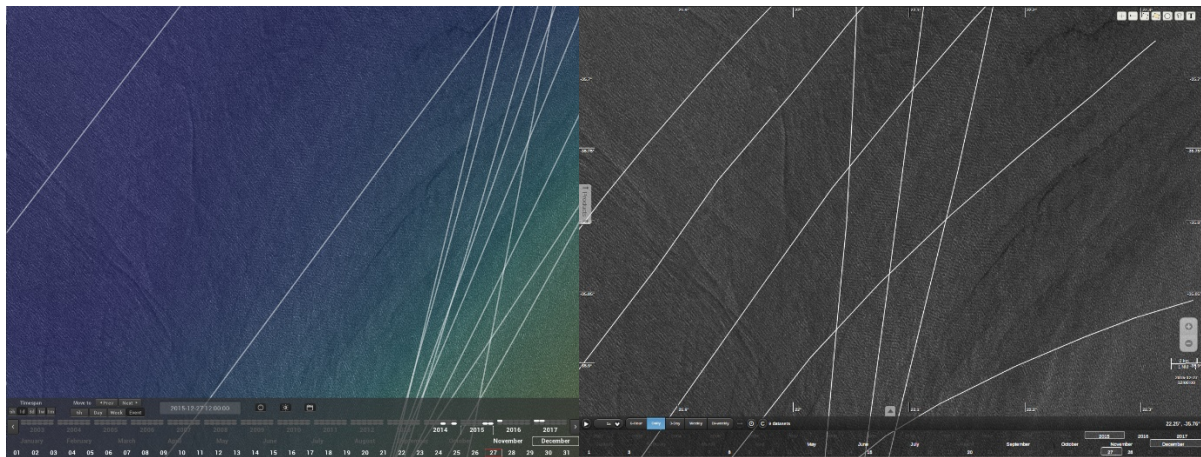


Figure A1.8: Swell propagation path simulated using GlobCurrent geostrophic current (left) and observed on Sentinel-1 SAR (right) overlaid on Sentinel-1 sea surface roughness map acquired on Dec. 27, 2015.

Annex 1.6: Spiraling Eddies

Spiral eddies were first seen in the sunglitter on the Apollo Mission in 1970 and have since been recorded in synthetic aperture radar (SAR) images as well as in infrared and ocean color images (Munk et al., 2000). They are 10-25 km in size and broadly distributed over the world's oceans, and they are overwhelmingly cyclonic. The features are wound into spirals in vortices associated with horizontal shear instability, modified by rotation, in regions where the horizontal shear is comparable with the Coriolis frequency. Under light to moderate winds the surface expression of these features can be recognized with high surfactant density and low surface roughness.

Spiral eddies manifest sub-mesoscale oceanographic processes and may constitute an important link in the balance of generating and dissipating ocean processes as illustrated in Figure 3b in the northern hemisphere and Figure A1.9 for the southern hemisphere.

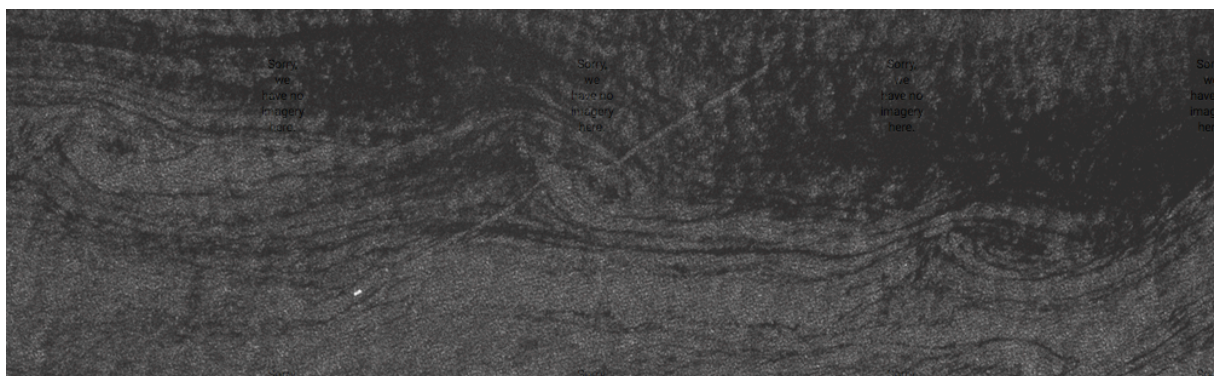


Figure A1.9: Train of spiraling cyclonic eddies in the Agulhas Return Current imaged by Sentinel-1 SAR on 21 November 2016. Note also the bright ship with the discontinuous ship track passing through the center of one of the spirals. Spiral sizes are 15-25 km.

According to Munk et al (2000) the formation of spiral eddies in the upper ocean with their distinct expression at the surface poses three basic questions that needs to be answered and explained:

- i. **How are the spirals wound?** Probably by the cat's-eye circulation associated with

horizontal shear instability. When the frontal shear becomes comparable with f , instabilities in the x, y -plane lead to cross-frontal flow accompanied by the development of a cat's eye circulation pattern that influence streaks of surfactants. The cat's-eyes circulation twists the convergence line and the neighboring linear features into a cyclonic spiral which stretches and further thins the lines of surfactant concentration. Almost any spiral pattern of particle distribution can be interpreted as a legacy of past vortex deformation.

- ii. ***How is symmetry broken in favor of cyclonic rotation?*** There are in fact many processes favoring the cyclonic rotation: (a) the relatively rapid development of super- f shear on the cyclonic side of frontal jets; (b) shear, static, centrifugal and inertial instabilities which selectively target the anticyclonic development of cat's-eye vortices. The central issue is not why there is a dominance of cyclonic eddies, but which of the proposed mechanisms limits the formation of anticyclonic vortices? An initial horizontal density transition in a thoroughly mixed layer with an imposed horizontal flow convergence develops into a jet with a strong cyclonic 'north wall' and a weak anticyclonic southern flank. The north wall eventually reaches vertical shear instability, but not until a horizontal shear of the order of $+3f$ has been attained. In comparison, note that RD-33 recently reported an upper ocean spiral with a vorticity of up to $+40f$. At the same time the anticyclonic vorticity is only $-0.5 f$ at most.
- iii. ***What makes the spirals visible?*** Most of the linear features seen on the halftone figures are wind streaks associated with atmospheric rolls, generated by winds prior to the relatively calm conditions favourable to detection in the sunglitter and in SAR images. Eddies are then visible through their action of twisting and straining these linear features, even without active frontal convergence. However, the frontal convergence that produces the shear, required for the subsequent cat's eye formation, will also produce shear lines. All lines in the near-field of the stagnation streamline, streaks and shear lines, accumulate onto the streamline and contribute to its visibility.

Annex 1.7: Synergy of Mesoscale Features

The synergetic approach combining SST, sun-glitter brightness and radar backscatter anomalies, augmented by other satellite data (e.g. altimetry, scatterometry, ocean color), can provide consistent and quantitative determination of the location and intensity of the surface current convergence/divergence (upwelling/downwelling) as demonstrated by [RD-8]. Combined with an advanced radar and/or optical imaging models this establishes an important step towards advances in the quantitative interpretation of the upper ocean dynamics associated with mesoscale features evidenced from their 2-D satellite surface expressions. This is illustrated in Figure A1.10 from a collection of satellite images obtained over the Greater Agulhas Current region displaying a distinct mushroom-like eddy pair. As noticed, it is visible in the SST field (Figure A1.10 a) and also clearly depicted in the surface current divergence field (Figure A1.10 b) inverted from the SST image and invoked into the radar imaging model (RIM). Together with the corresponding sun glitter derived MSS field (Figure A1.10 c) and the SAR NRCS contrasts (Figure A1.10 d) of the mushroom like eddy-pair, acquired 5 hours apart, this provides a striking demonstration of the strength in the proposed satellite sensor synergy and interpretation framework. The textural agreement in the observed SST, NRCS and MSS surface expressions together with the surface convergence map, in particular for the anticyclone eddy, provides clear evidence that the synergetic approach strengthen the quantitative analyses of the upper ocean dynamics.

The direct interaction of the non-divergent quasi-geostrophic current (QGC), reconstructed from the SST field, with the wind waves results in weak surface manifestation of mesoscale

current features. On the other hand, the interaction of the wind driven upper layer motion with the QGC field (via Ekman advective and mixing mechanisms, as suggested by [RD-16] and [RD-17]) can generate sufficiently strong ageostrophic surface current (see eq. 8), that, in turn, produces intense surface current convergence and divergence. Under the proposed assumption, intense cross-frontal dynamics occur near sharp horizontal gradients of the vorticity of the QGC, as well as strong vertical gradients of the QGC velocity.

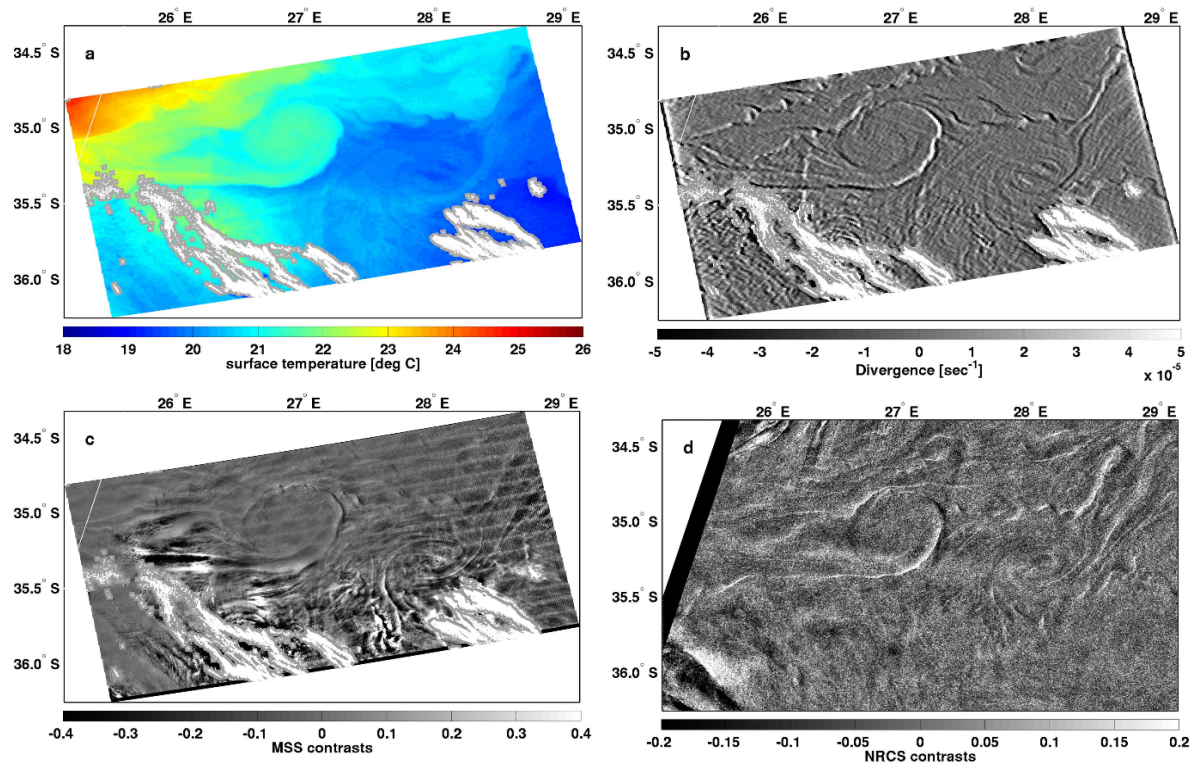


Figure A1.10: Multi-sensor expressions of a mushroom like eddy pair with a diameter of 120 km. MODIS SST map (a) and surface current divergence field derived from the SST field (b). The MSS contrasts derived from the MODIS (c) and the ASAR NRCS contrast (d). The NRCS contrasts are in linear units. Bright areas in the upper-right plot correspond to the current convergence, and dark – to the current divergence.

Accordingly, one may consider the observed striking agreement and correspondence between roughness anomalies and SST gradients as “an experimental evidence” of the fact that the impact of the surface current divergence on the short wind waves constitutes the governing mechanism leading to manifestation of mesoscale surface current features in the form of the “surface roughness” anomalies. On the other hand, the correlation between the surface roughness anomalies and the model surface current divergence strongly suggests that the model framework for the reconstruction of the mesoscale surface current is quite reliable, as also demonstrated during the large drifter deployment experiment undertaken in the Gulf of Mexico in February 2016 [RD-33].

Annex 1.8: Snapshot Examples from SynTool

All Globcurrent products from 1993 to 2016 can be visualized using the GlobCurrent data portal <http://globcurrent.oceandatalab.com/>. The viewing options range from global to regional and offers a wide span of product collocations and overlaying possibilities. The selection of products to be displayed is controlled by the “Products” while the date and time

selection is controlled a timeline panel. The visibility of snapshots products at different times can be controlled by changing the time window duration centered on the current date from 6 hours to 3 months. This interface is meant to be intuitive with tooltips available and can also be controlled using Keyboard “Shortcuts”. The “Settings” menu can be used to control transparency, layer ordering, color bars, and advanced filters. The “Share” button generates a short URL permalink that can be used to share the same view of the portal to somebody else. In Figure A1.11a and Figure A1.11b the coincident SST and Ocean Color images from the Benguela upwelling region and the Agulhas Current are depicted for two December 2015 cases (respectively 17 and 23 December).

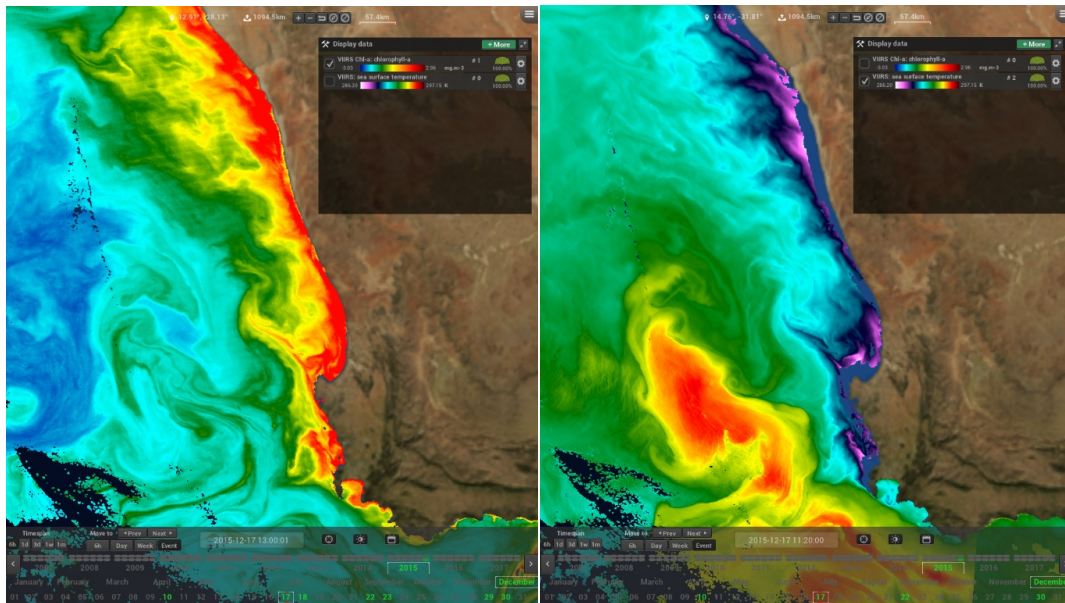


Figure A1.11a: Collocated Chl-A concentration (left) and SST field (right) from VIIRS radiometer showing negative correlation in the Benguela coastal upwelling region.

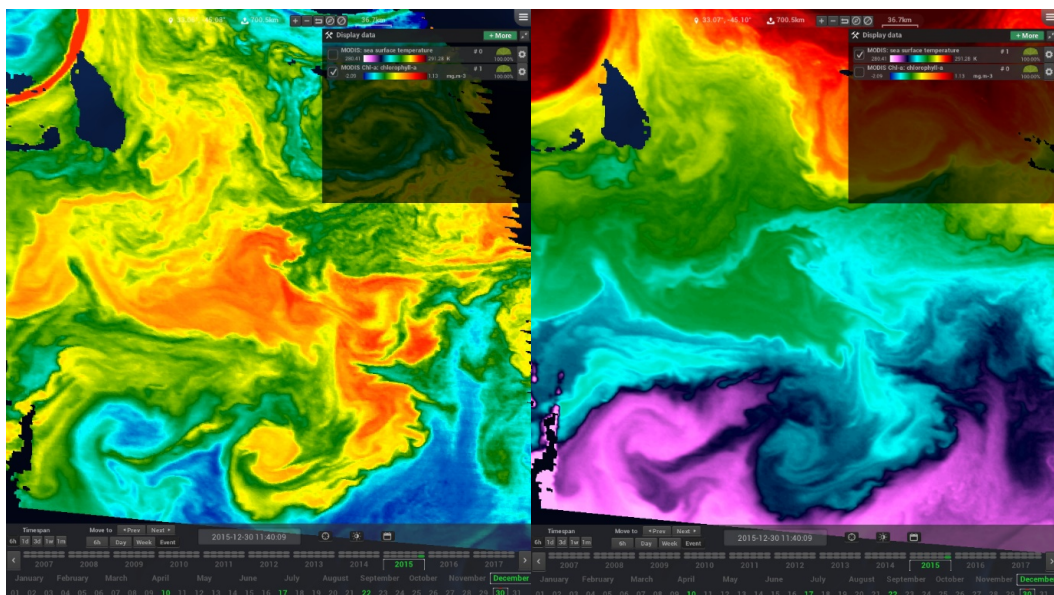


Figure A1.11b: Collocated Chl-A concentration (left) and SST field (right) from MODIS radiometer showing positive correlation in the eddies shed from the Agulhas Return Current into the Antarctic Circumpolar Current.

The pair of images displays distinctly different relationships of the SST and Chlorophyll A distribution within the mesoscale eddies. Whereas a clear anti-correlation is found for the Benguela case with warm SST and low Chlorophyll A concentration the situation in the ACC is completely opposite with a high Chlorophyll A patch found jointly with relatively warm water (as compared to the surroundings). Based on such images and eventually the use of the Lagrangian propagation method it might be feasible to investigate and quantify the relative importance of the advective versus convective dynamics that have shaped the surface expressions of these mesoscale features.

Annex 1.9: From Symbology to Synoptic Maps

Symbology is used to synthesize the information content in observation snapshots to create a synoptic map representing the surface current boundaries and the associated main current flow pattern for a given time window. The validity of such a map is dependent on the regional dynamic regime and may vary from about 1 day in the Mediterranean Sea to 3 days in the Agulhas Current and to 1 week or more in the equatorial region. Such synoptic maps can then be used to validate or modify surface current forecast from oceanic circulation model in order to derive optimized and qualified forecast for practical applications such as Search and Rescue and or Ship routing as shown in Figure A1.12.

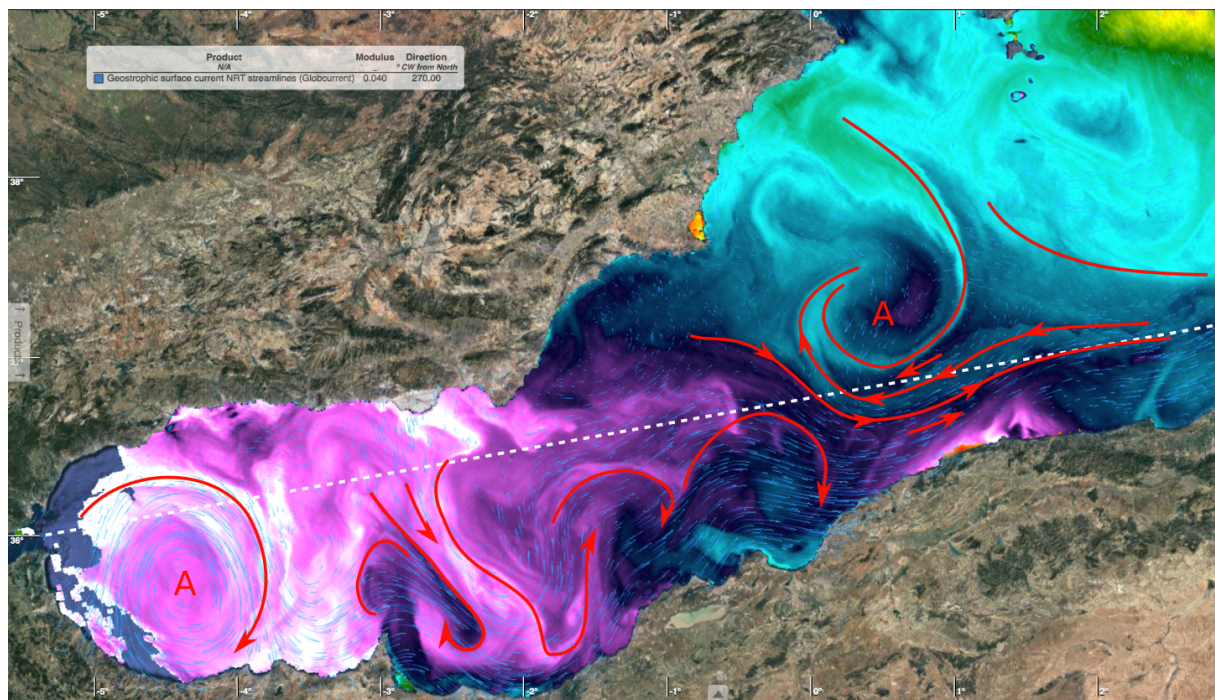


Figure A1.12: The western Mediterranean Sea has a variety of features that can be used to optimize ship routing. Part of the challenge is to delineate and extract high-level features of interest such as water-type boundary fronts and significant currents of interest for a particular ship voyage. This image shows sea-surface temperature overlaid with GlobCurrent streamlines. The white broken line shows the planned passage of a ship that takes advantage of ocean-surface currents.